Conceptual Design Report on a HBD Upgrade for the PHENIX Detector

B. Azmoun[a], L. Baksay[c], C.Y.Chi[b], A. Drees[g], A. Dubey[i], Z. Fraenkel[i], J. Franz[g], M. Grosse-Perdekamp[f,d], H. Hamagaki[h], J. Harder[a], T. Hemmick[g], M. Hohlmann[c], R. Hutter[g], B. Jacak[g], D. Kawall[f,e], A. Kozlov[i], D. Lynch[a], M. McCumber[g], A. Milov[g], M. Naglis[i], P. O'Connor[a], S. Oda[h], K. Ozawa[h], R. Pisani[a], V. Radeka[a], I. Ravinovich[i], S. Rembeczki[c], D. Sharma[i], A. Sickles[g], A. Toia[g], I. Tserruya[i], C. Woody[a], W. Xie[f], B. Yu[a].

[a] Brookhaven National Laboratory, Upton NY 11973-5000, USA

[b] Columbia University, New York, NY 10027, USA

[c] Florida Institue of Technology, Melbourne FL 32901, USA

[d] University of Illinois, Urbana-Champaign, Urbana, IL61801, USA

[e]University of Massachusets, Amherst, MA 01003, USA

[f]RIKEN-BNL Research Center, Brookhaven National Laboratory, Upton NY 11973-5000, USA

[g]Stony Brook University,, Stony Brook, SUNY, NY 11794-3400, USA

[h]University of Tokyo, Tokyo 162-0044, Japan

[i]Weizmann Institute of Science, Rehovot 76100, Israel

Contents

1 Executive Summary

We propose to add to the PHENIX central arm spectrometer a Hadron Blind Detector (HBD) for the measurement of electron pairs particularly in the low-mass region (m $<$ 1 GeV/c^2). This is an exclusive niche of PHENIX. No other experiment at RHIC can perform this measurement.

Dileptons are valuable probes to the diagnoe of the hot and dense matter formed in ultra-relativistic heavy-ion collisions. They play a crucial role in the quest for the QCD phase transition to the Quark Gluon Plasma (QGP) expected to be formed in these collisions. They can provide fingerprint evidence of chiral symmetry restoration and deconfinement which are the two fundamental characteristics of the QGP.

The physics potential of this probe is fully confirmed by results from low energy experiments. All completed dilepton experiments in heavy-ion collisions (DLS, P235, CERES, HELIOS-3, NA38/50) have produced very interesting and intriguing results. The most prominent result is the enhancement of low-mass electron pairs observed by the CERES experiment at CERN SPS in all heavy-ion collision systems studied. This enhancement triggered a wealth of theoretical activity and was quantitatively reproduced only by invoking the thermal radiation from a high density hadron gas ($\pi^+\pi^- \rightarrow \rho \rightarrow \gamma^* \rightarrow e^+e^-$) with an in-medium modification of the intermediate ρ meson which could be linked to chiral symmetry restoration.

The prospects at RHIC look very promising. The total baryon density, which is the key factor responsible for the in-medium modifications of the ρ meson at SPS energies, is almost as high at RHIC as at SPS, due to the copious production of baryon-antibaryon pairs at RHIC. Furthermore, the temperature factor which played a minor role at SPS energies is expected to be more significant at RHIC energies. Recent calculations predict indeed that the enhancement of low-mass electron pairs persists at the collider with at least a comparable strength. In addition to the ρ, the calculations also predict strong in-medium modifications of the ω and ϕ mesons. These are much less dramatic than in the case of the ρ meson but could nevertheless be observable with the excellent mass resolution of the PHENIX detector.

Dileptons offer also the possibility to identify the thermal radiation emitted from the QGP via $\bar{q}q$ annihilation. Such a radiation is a direct identification of the matter formed and is regarded as a very strong signal of deconfinement. There is no convincing evidence for thermal radiation from the QGP at lower energies, either in the dilepton or in the real photon channels. Theoretical calculations have singled out the dilepton intermediate mass range (m = 1-3 GeV/c^2) as the most appropriate window for the observation of the QGP thermal radiation.

The measurement of electron pairs is however a very challenging one. The main difficulty arises from the huge combinatorial background created by π^0 Dalitz decays and γ conversions. For example with the present PHENIX configuration the signal to background ratio, S/B, at an invariant mass of m$\sim$ 500 MeV/c^2 is approximately 1/500 making the measurement of the low-mass pair continuum practically impossible.

The HBD upgrade that we are proposing reduces this background by at least two orders of magnitude. Its main task is to identify and reject pairs from π^0 Dalitz decays and γ conversions with an efficiency of at least 90%. The HBD is installed close to

the vertex in the almost field free region created by the two coils operated in the +- configuration.

The HBD is a windowless Čerenkov detector, operated with pure CF_4 in a proximity focus configuration. The detector consists of a 50 cm long radiator directly coupled to a triple-GEM detector which has a CsI photocathode evaporated on the top face of the first GEM foil and a pad readout at the bottom of the GEM stack. In this scheme the Čerenkov light from particles passing through the radiator is directly collected on the photocathode forming a circular blob image rather than a ring as in a RICH detector.

Over the past two years we have carried out a comprehensive R&D program to address issues and questions raised by this novel scheme. We have shown that a triple GEM detector with a reflective CsI photocathode operates in a stable mode at gains up to 10^4 in pure CF_4. We found a charge saturation effect in CF_4 when the total charge in the avalanche reaches 4×10^7 e making the HBD relatively robust against discharges. We carried out a test of a triple-GEM detector operated with pure CF_4 at the proposed location inside the PHENIX central arm spectrometer. The detector performed smoothly in the presence of Au+Au collisions exhibiting no discharges or gain instabilities. We have studied the basic parameters which determine the HBD performance. In particular, we measured the device response to mips and to electrons. Large hadron rejection factors, well in excess of 100, can be achieved while preserving an electron detection efficiency larger than 90%. We confirmed measurements of the CsI quantum efficiency over the bandwidth 6-8.3 eV and extended them up to 10.3 eV. Extrapolation to the expected operational bandwidth of the device (6-11.5 eV) gives a figure of merit N_0=822 cm^{-1} and $\sim$ 36 photoelectrons over a 50-cm long radiator. Aging studies of the GEM foils as well as the CsI photocathode revealed that there is no significant deterioration of the detector for irradiation levels corresponding to $\sim$ 10 years of normal PHENIX operation at RHIC. These results demonstrate the validity of the proposed HBD concept and pave the way to the incorporation of such a device in the PHENIX experiment.

The mechanical design of the HBD has been developed and construction procedures have been exercised and optimized on a full-scale prototype. The HBD is made of two identical arms, each one covering 135^o in azimuth and ±0.45 units of pseudorapidity. In each arm the detector element is subdivided in 12 detector modules, 6 along the ϕ axis $\times$ 2 along the z axis, with a module size of $\sim 23 \times 27$ cm^2. The signals are collected in the anode plane consisting of 1152 hexagonal pads in each arm. The detector vessel has a polygonal shape made of panels glued together. The full-scale prototype design has been integrated into the PHENIX standard simulation package (PISA). Realistic simulations have been performed using HIJING central Au+Au collisions at $\sqrt{s_{NN}} = 200$ GeV with embedded ϕ mesons. With a simple HBD pattern recognition algorithm, the combinatorial background originating from π^0 Dalitz decays and γ conversions is reduced by more than two orders of magnitude compared to the present performance without the HBD. At this level of rejection the quality of the low-mass pair measurement is not anymore limited by this background but rather by the combinatorial background from the semi-leptonic decays of charmed mesons.

There are preliminary plans to derive from the HBD not only an electron trigger for the measurement of low-mass electron pairs but also a high-p_T charged-hadron trigger in polarized pp collisions.

The HBD construction will take place at the Weizmann Institute (detector vessel, assembly and preliminary test of GEM foils) and at Stony Brook University (CsI evaporation, assembly and test of detector modules) and will be carried out mainly by students from CNS, FIT, SBU and WI. The electronics is developed and built by BNL Instrumentation (analog) and Columbia University (digital and trigger). The total cost of the device is estimated at $\sim$ \$1,100,000 based on realistic quotes and reasonable contingency. We are proposing an aggressive but doable schedule that will allow us to have the HBD ready at the beginning of year 2006.

2 Physics Motivation for a Hadron Blind Detector

During the first 10 microseconds following the Big Bang, the temperature of the universe was so high that the dominant form of matter was unbound quarks and gluons in a state referred to as quark-gluon plasma. Such a plasma interacts via the strong interaction, rather than electromagnetic, but is expected to manifest many of the same features as classical plasmas, such as screening and collective effects. The extraordinarily high temperature of the epoch just after the Big Bang, is achievable today only in collisions of heavy nuclei at relativistic energies. The energy density of this kind of matter far exceeds that of normal nuclear matter, and indeed of other plasmas currently accessible.

We probe this kind of matter using the PHENIX experiment at the Relativistic Heavy Ion Collider (RHIC) at Brookhaven National Laboratory. While the lifetime of the fireball is only about 1.5-3.0 x 10^{-23} sec, precision probes of the plasma state generated early in the collision by high momentum transfer scattering of quarks and gluons in the incoming nuclei can be used to map the evolution of the matter. To find the properties of this new kind of plasma, it is important to determine its temperature, collision frequency, thermal conductivity, color dielectric properties, radiation rate, radiative-absorptive coefficients and opacity. First glimpses into many of these properties are becoming available from the data collected at RHIC so far. However, there is as yet no experimental information whatsoever about the temperature reached by the plasma. Measuring this temperature requires detecting thermal radiation consisting of real or virtual photons emitted by the plasma.

As the universe cooled down from the quark gluon plasma state to a temperature of approximatly 200 MeV the vacuum ground state became filled with a condensate of quarks that spontaneously broke the chiral symmetry present at high temperature, giving rise to hadron masses which are large compared to the masses of light quarks. The underlying mechanism which connects symmetry breaking, mass generation and ground state properties is thought to account for more than 90 % of the visible mass in the Universe. However, experimental evidence for chiral symmetry restoration at RHIC has not yet been found. The most promising way to search for this evidence is to measure low-mass dileptons from decays of vector mesons inside the hot, dense medium.

Indeed, photons and dileptons have long been considered promising signals of the physics of the early stage of heavy-ion collisions. When the temperature and density are highest, the thermal radiation rate is maximal. As the hot, dense fireball approaches the transition back to hadronic matter with broken chiral symmetry, hadronic resonances form, albeit with properties modified compared to their vacuum values. However, to date, the high backgrounds from π^0 Dalitz decays and γ conversions have prevented reliable measurements of either process. We aim to solve this problem with a novel detector technology, directly measuring and rejecting electrons and positrons from π^0 Dalitz decays and γ conversions. This will allow detection of electron-positron pairs from virtual photons, and search for evidence of chiral symmetry restoration via electron-positron pairs from the decay of unstable hadronic resonances. In particular, decays of ρ ,ω and ϕ allow study of medium-induced changes of the resonance masses and widths, as the electrons and positrons do not interact with the surrounding medium. Since resonance masses trace the chiral symmetry order parameter, their measurement addresses directly

the origin of chiral symmetry breaking.

2.1 Physics Measurements via Low Mass Lepton Pairs

Thermal dileptons populate the continuum region of the e^+e^- or $\mu^+\mu^-$ invariant mass spectrum, and in the absence of non-thermal backgrounds, the tail of the transverse momentum spectrum of such pairs reflects the initial temperature T_{init} achieved in the collision. The mass range of interest is fixed by the temperature of the system, but typically extends from T_{init} to 4 or 5 times T_{init}, i.e. from a few hundred MeV to 1.5 or 2 GeV at RHIC. Unfortunately, nature is not kind enough to provide a classic thermal radiation spectrum in particle collisions. In the e^+e^- mass spectrum measured in p+p collisions there are peaks arising from the leptonic decays of hadrons, Drell-Yan lepton pairs contributing a high mass continuum, and complex hadronic decays that populate the other continuum regions. The latter are primarily Dalitz decays of π and η mesons feeding into the low mass dilepton region, and charmed meson decays contributing at intermediate masses.

In heavy-ion collisions, the mass spectrum above should be modified. In addition to the expected presence of thermal radiation, vector meson masses and widths, especially for the low-mass ρ meson, may be modified due to chiral symmetry restoration and/or multiple interactions with neighboring particles in a dense medium. The production of charmed quarks may be enhanced in high temperature matter, leading to an increased yield of intermediate mass continuum lepton pairs. The yield of J/Ψ may decrease significantly if color screening is present, decreasing the potential between produced $c\bar{c}$ pairs.

Onset of chiral symmetry restoration should lower the mass of mesons inside the dense medium [1]; as the lifetime of the ρ is short, many ρ-s decay while the temperature and density of the medium are large. The dilepton spectrum should then reflect the in-medium mass, as the decay leptons do not interact with the medium on their way to the detector. It has alternatively been suggested that collisional broadening in a dense medium may affect the observed width and mass of vector mesons [2]. Such an effect would open additional phase space below the vacuum lepton mass. Both mechanisms lead to additional dileptons around 500 MeV/c^{2}mass compared to that in p+p collisions. Indeed, excess dilepton yield in this mass region was observed in heavy-ion collisions by the CERES collaboration at the CERN SPS [3], as illustrated in Fig. 1. The dotted lines show the expected sources of di-electrons from various hadronic decays; their sum (thin solid line) clearly underpredicts the data. The dashed line shows the expected contribution from unmodified ρ-mesons (including feeding of the channel from $\pi^+\pi^-$ collisions in the hadronic medium), and is incompatible with the measurement. The heavy solid line and dot-dashed line show expectations from broadened and lowered-mass ρ mesons, respectively, and are closer to the data. The CERES measurement provides clear evidence for medium modification of vector mesons, but has inadequate statistical precision and mass resolution to constrain the extent or type of modification. The data do show, however, that the mass region between 0.3 and 1 GeV/c^2 provides the best sensitivity to medium-modification effects.

Experiments have also measured dileptons in lower energy heavy ion collisions at the Bevalac, and in 12 GeV proton-nucleus collisions at KEK. The KEK experiment probed the effect of cold nuclear matter upon vector meson masses and widths, and found that

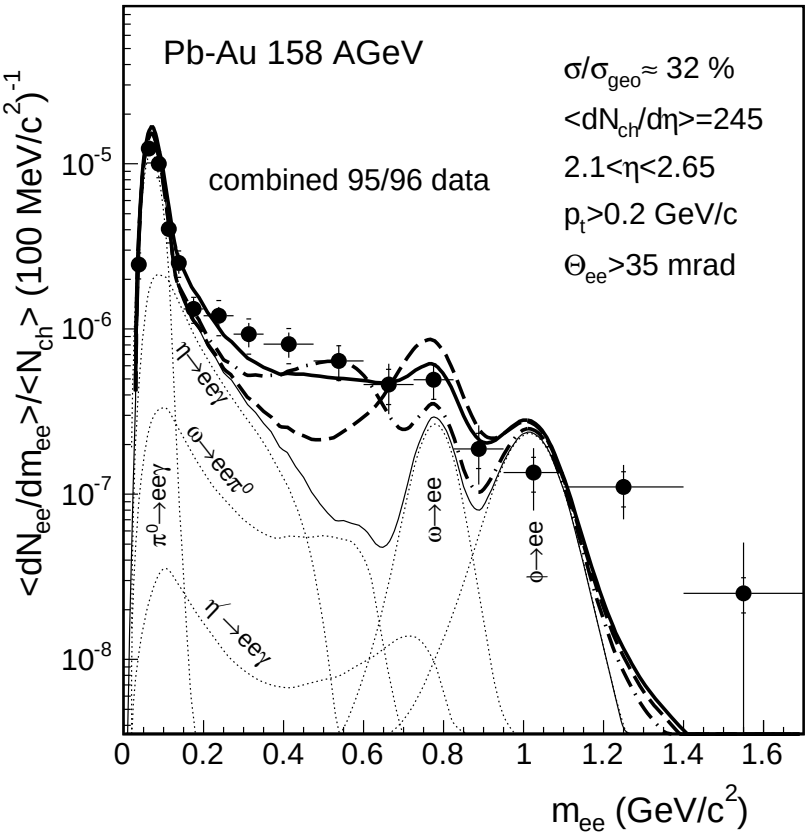

Figure 1: Invariant mass spectrum of electron-positron pairs measured by the CERES collaboration at the CERN SPS.

the dilepton spectrum in p+C and p+Cu collisions cannot be fit using vacuum ρ mass and width from the Particle Data Group [4]. Furthermore, the ϕ mass region showed clear differences between C and Cu targets. Intriguingly, the observed dilepton spectra can be reproduced by assuming that ρ and ω mesons are produced at the nuclear surface, and decay with decreased mass if the decay point is inside the nucleus. However, it is not at all clear that this explanation of the preliminary data is unique. The DLS experiment at the Bevalac measured low mass dilepton production in 1 GeV/A Ca+Ca collisions [5]. The measurement below 1 GeV invariant mass could not be reproduced by calculations incorporating hadronic decays with unmodified ρ spectral functions [6]. Dilepton production was observed to be significantly enhanced, even when including the in-medium ρ spectral function. The need to understand this puzzle prompted development of the HADES experiment at GSI.

To summarize, all the lower energy results have shown strong differences from the dilepton spectra in p+p collisions, and motivate making a good, clean measurement of low-mass dileptons at RHIC.

2.2 Dilepton Production Expected at RHIC

A number of theoretical studies of conditions in RHIC collisions and their effect upon dilepton spectra have been carried out. These calculations use experimental observations to constrain assumptions about the early stage, including large final baryon and anti-baryon yields, high initial energy density (and therefore initial temperature, T_{init}), large expansion velocity, and evidence for short lifetime of an equilibrated, cooler hadronic phase. Unlike at SPS energy, where T_{init} is lower and the hadron gas phase rather long-lived, at RHIC the plasma is predicted to outshine the hadron gas with real photons of energy 1-3 GeV [7]. Rapp has calculated the contributions to dilepton spectra from various sources, including decay of medium-modified mesons, the results are shown in Fig. 2 [8]. Thermal dileptons dominate the low-mass continuum, though the relative contribution from plasma and hot hadron gas phases depend strongly on the relative lifetimes and T_{init}. Nevertheless, a strong thermal contribution to low-mass lepton pairs is predicted. An interesting point to note is that the total baryon rapidity density at RHIC is comparable to that at the SPS, even though the net baryon density is lower. Consequently, modifications of resonance masses and widths are expected at RHIC as well. At intermediate masses, open charm decays constitute a significant background, but this can be subtracted once the charm spectrum is measured.

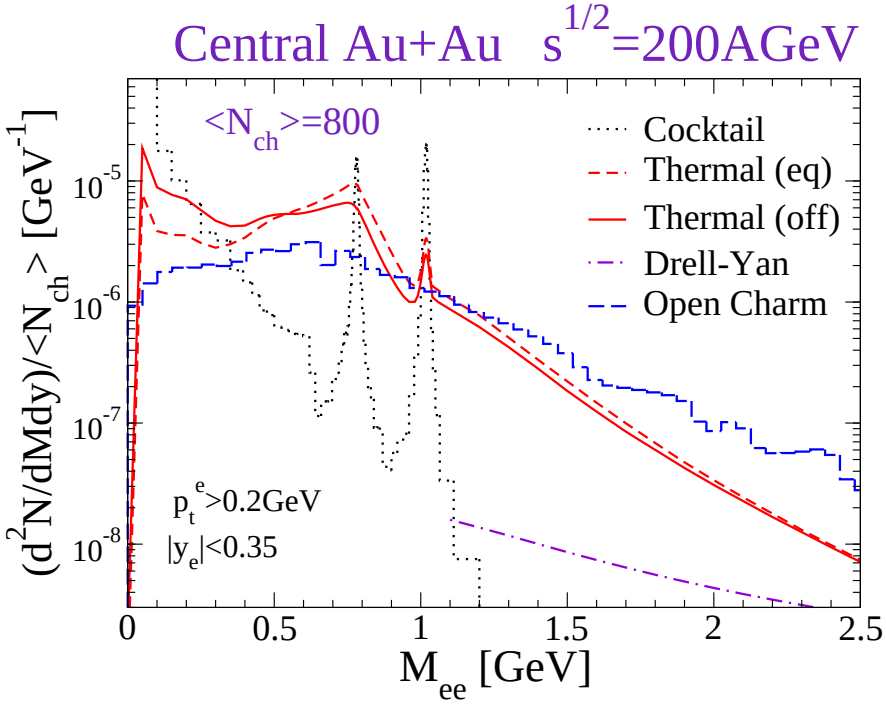

Figure 2: Predicted dilepton mass spectrum at RHIC.

.

It should be noted that the quark gluon plasma at RHIC appears to be strongly coupled [9, 10]. This implies a large probability for formation of quasi-bound states at the temperatures accessible at RHIC of approximately 2 T_c [10], and indeed evidence for such bound states has been seen in the spectral functions of quarks in high temperature

lattice QCD studies for heavy and strange quarks [11]. Non color-neutral bound states of light quarks may also exist [10]. The existence of such states in the plasma could have profound effects upon the dilepton spectrum, adding new peaks at masses determined by the temperature of the plasma and thermal masses of quarks in the strongly-coupled medium. As the strength of such peaks may not necessarily be large, dilepton background is crucial to any search for these phenomena. The apparent short lifetime of the equilibrated hadron gas phase late in the collision suggests that strongly coupled plasma effects may exceed thermal radiation from the hadronic phase, however, experimental data is crucial and currently non-existent.

2.3 Need for Hadron Blind Detector

The measurement of electron pairs is a very challenging one. In order to examine the very interesting features of the dilepton mass spectrum, measure the yield and distribution of thermal dileptons and observe expected modifications to meson masses from chiral symmetry restoration, the combinatorial background must be suppressed. The limited azimuthal angular acceptance in the central arms and the strong magnetic field beginning radially at R=0, makes the identification and rejection of electron-positron pairs from Dalitz decays and photon conversions very difficult. The large number of electrons and positrons from these sources produces an overwhelming combinatorial background. Fig. 3 shows the electron-positron invariant mass spectrum from an analysis of the 2002 Au+Au data, after subtraction of the large combinatorial background determined from mixed events with an electron from one event and positron from a different event. The signal to background ratio is of the order of S/B $\sim$1/200 (1/500) with a single electron p_T cut of 300 (200) MeV/c. It is clear that the statistical and systematic uncertainties in the low-mass region are huge, and simply increasing the statistics will be insufficient to allow a useful measurement. Improvement of the signal to background ratio is imperative.

The strategy adopted by the PHENIX Collaboration and the aim of the present proposal is to use a Hadron Blind Detector to reconstruct and reject Dalitz decays and conversion pairs. This together with the excellent mass resolution of PHENIX will increase the sensitivity to small in-medium modifications of the known resonances The HBD will also improve the signal to background ratio in the intermediate mass region. The charm decay background in this region will be measured using a highly segmented silicon microvertex detector to tag vertices displaced from the collision vertex for electrons from semi-leptonic decays. Finally there are preliminary plans to use the HBD as high-p_T hadron trigger in polarized pp collisions.

3 The HBD Concept

The PHENIX detector was designed anticipating that the measurement of low-mass pairs would be feasible with an appropriate upgrade. In particular, provision was made for the installation of an inner coil which would create an almost field-free region close to the vertex, extending out to $\sim$50-60 cm in the radial direction. In addition to this coil (which was installed in PHENIX for Run 4), the major and challenging element of the

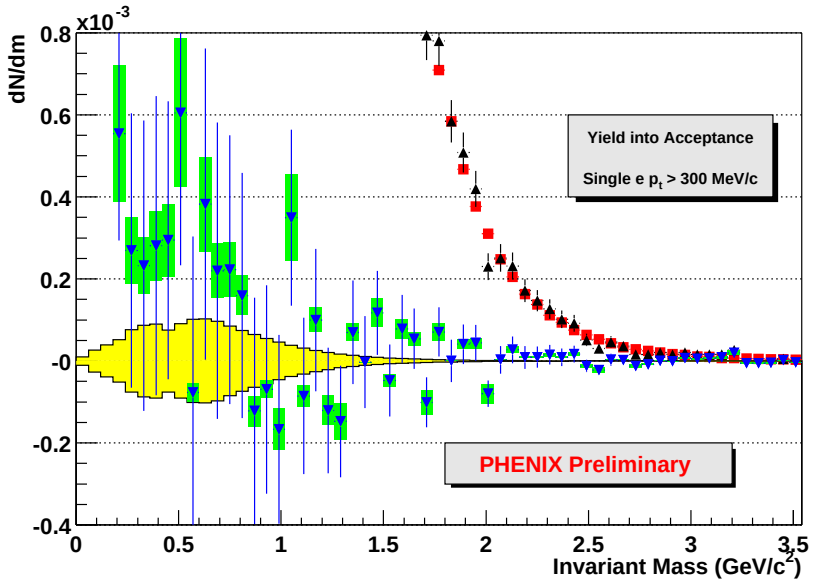

Figure 3: Low-mass dilepton mass spectrum from analysis of Au+Au data after subtraction of the combinatorial background from mixed events with an electron from one event and positron from a different event.

upgrade is a hadron-blind detector (HBD) located in this field free region. The main task of the HBD is to recognize and reject γ conversions and π^o Dalitz decays. The strategy is to exploit the fact that the opening angle of electron pairs from these sources is very small compared to the pairs from light vector mesons. In the field-free region, this angle is preserved and by applying an opening angle cut one can reject more than 90% of the conversions and π^o Dalitz decays, while preserving most of the signal. The size of the HBD is constrained by the available field-free region starting outside the beam pipe (at r$\sim$5 cm) and ending at the inner coil (at r$\sim$60 cm). Fig. 4 shows the layout of the inner part of the PHENIX detector together with the location of the coils and the proposed HBD.

In [12] we performed conceptual Monte Carlo simulations at the ideal detector level, to quantify the potential benefit and define the system specifications, of the HBD. The most important aspects of this study are described in Appendix A and the main findings are summarized here. A reduction of the combinatorial background originating from conversions and π^0 Dalitz decays of at least two orders of magnitude can be achieved with a detector that provides electron identification with a very high efficiency, of at least 90%. This also implies a double (electron) hit recognition at a comparable level. On the other hand, a moderate π-rejection factor of $\sim$100 is sufficient. It is also important to have a larger acceptance in the HBD compared to the fiducial central arm acceptance to provide a veto area for the rejection of pairs where only one partner is inside the fiducial acceptance. At this level of rejection, the quality of the low-mass e^+e^- pair measurement is not any longer limited by the background originating from γ conversions and π^o Dalitz decays but rather by the background originating from semi-leptonic decays of charmed mesons.

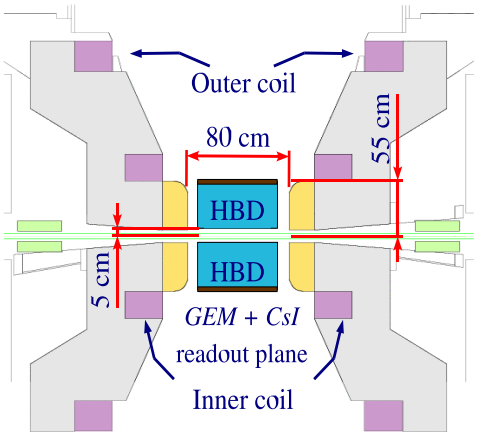

Figure 4: Layout of the inner part of the PHENIX detector showing the location of the HBD and the second coil.

In [12] we analyzed possible realizations of the HBD detector. The requirements on electron identification limit the choice to a Čerenkov-type detector. Since a mirror-type RICH detector in the center of PHENIX is very difficult or nearly impossible to implement, we consider a scheme without mirror and without window in which the Čerenkov light from particles passing through the radiator is directly collected on a CsI photosensitive cathode plane, forming a circular blob image rather than a ring as in a RICH detector. After careful consideration of relevant options for the key elements (gases, detector configuration and readout chambers), we adopted the following scheme for the HBD: a windowless Čerenkov detector, operated with pure CF_4 in a proximity focus configuration, with a CsI photocathode and a triple-GEM detector [13] element with pad readout.

This scheme exhibits a number of very attractive features:

- The choice of CF_4 both as radiator and detector gas in a windowless geometry results in a very large bandwidth (from ∼6 eV given by the threshold of CsI to ∼11.5 eV given by the CF_4 cut-off) and consequently in a very large figure of merit N_0 which was estimated in [12] to be close to 900 cm^{-1}. With these unprecedented numbers, the number of photoelectrons N_{pe} is expected to be of the order of 40 for a 50 cm long radiator (after including losses incurred by the optical transparency of the entrance mesh and the GEM-photocathode) [12]. This large value of N_{pe} ensures a very high electron efficiency, and more importantly, it is crucial for achieving a double-hit resolution larger than 90%.

- Another important advantage of the present design using GEMs is that it allows the use of a reflective photocathode. In this scheme, the top face of the first GEM is coated with a thin layer of CsI and the photoelectrons are pulled into the holes of the GEM by their strong electric field. Consequently, the photocathode is totally screened from photons produced in the avalanche process.

- The readout scheme foresees the detection of the Čerenkov photoelectrons in a pad plane with hexagonal pads of size slightly smaller than the blob size ($\sim$10 cm^2) such that the probability of a single-pad hit by an electron entering the HBD is negligibly small. For example, with hexagonal pads of side a = 1.56 cm, 96.9% of the electrons will produce a hit with at least two pads. On the other hand, whenever a hadron gives a signal in the HBD, it will produce a single pad hit with an almost 100% probability. This will provide a strong handle in the hadron rejection factor of the HBD.

- The relatively large pad size results also in a low granularity and therefore a low cost detector. In addition, since the photoelectrons produced by a single electron will be distributed between at most three pads, one can expect a primary charge of at least 10 electrons/pad, allowing the operation of the detector at a relatively moderate gain of a few times 10^3. This is a crucial advantage for the stable operation of a UV photon detector.

4 HBD R&D Results

The concept described in the previous section is very attractive. However, many elements of the proposed HBD were new and had not been tested before in the laboratory. A number of issues and questions were raised which required dedicated investigation. In particular, no experiment has ever used pure CF_4 as operating gas. Stable operation of a triple GEM structure in CF_4 at gains of 10^4 had to be demonstrated. Aging effects on the GEM foils and the CsI photocathode had to be studied. The main concern is the aggressiveness of CF_4 and HF that can be formed by chemical reactions of CF_4 with water. Ion back-flow effects on the photocathode had also to be studied. No data existed on the CsI quantum efficiency beyond 8.5 eV. Finally the HBD response to hadrons and electrons had to be studied and optimized. To address all these questions and to demonstrate the concept validity, we have carried out over the past two years a comprehensive R&D program. The results of this effort are published in [14, 15, 16] and are presented in this section.

4.1 Setup and Experimental Conditions.

For all the measurements, GEMs produced at CERN were used with 50 μm kapton thickness, 5 μm thick copper layers, 60-80 μm diameter holes and 140 μm pitch. The GEMs had 3×3 or 10×10 cm^2 sensitive areas. These two types of GEMs will be referred to in the text as "small" and "large" respectively. Three GEMs were assembled in one stack with G10 frames as shown in Fig. 5. The distance between the GEMs was 1.5 mm and the distance between the bottom GEM (GEM3) and the printed circuit board (PCB) was in most (some) cases 2 mm (1.5 mm). The distance between the top GEM (GEM1) and the drift mesh was 3 mm in the measurements with X-rays and α-particles and 1.5 mm in the measurements with UV-photons.

The PCB consisted of 5 stripes of 100×20 mm^2 each. The central stripe was connected either to a charge sensitive pre-amplifier and shaper or to a picoammeter, depending on

the particular measurement. The other stripes were grounded.

Two gases were used for the measurements: an Ar/CO_2 (70/30%) mixture and CF_4. We used a premixed bottle of Ar/CO_2 with Ar of 99.999% purity and CO_2 of 99.998% purity. The purity of the CF_4 was 99.999%.

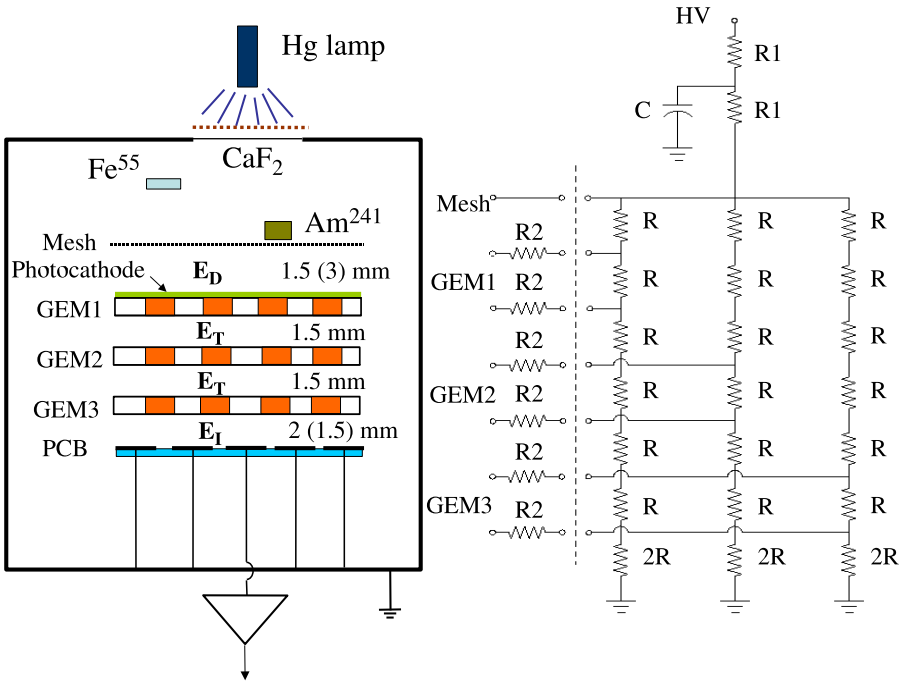

Figure 5: Setup of the triple GEM detector and resistor chain. The Hg lamp, ^{55}Fe and ^{241}Am sources were used for measurements with UV-photons, X-rays and α-particles, respectively. The two values for R1 and E_I are explained in the text.

In the following we refer to the gap between the mesh and top GEM as "drift"-gap, the gaps between GEMs are called "transfer" and the gap between GEM3 and the PCB is called "induction". The corresponding fields are E_D, E_T, and E_I. Most measurements were performed with a 2 mm induction gap and a 20 MΩ resistor feeding the gap. In this configuration, when the voltage across the GEMs is 510 (370) V, corresponding to a gain of $\sim$ 10^4 in CF_4 (Ar/CO_2), the transfer and induction fields are about 3.4 (2.5) kV/cm and 5.1 (3.7) kV/cm, respectively. When R1 is equal to 10 MΩ, the induction fields are half the quoted values.

The photocathode was prepared by evaporating a $\sim$ 2000Å thick layer of CsI on the first GEM, previously coated with thin layers of Ni and Au to avoid chemical reaction with the CsI film. For the operation with the reflective photocathode the drift field has to be zero or even reversed in order to collect all the photo-electrons from the CsI layer [17]. For those measurements the corresponding resistor in the chain was shorted. The measurements with the CsI reflective photocathode were performed with a Hg lamp and a UV-transparent window (CaF_2) in the cover of the detector box. The lamp was positioned at the detector window with an absorber that reduced the UV flux$\sim$1000 times to avoid possible damage of the photocathode [18]. The illuminated area of the detector

was about 100 mm^2. In this geometry, the measured photo-electron current was about 2×10^6 e/mm$^2\times$s. The quantum efficiency of the CsI photocathode was $\sim$10% at 185nm.

The detector assembly (drift mesh, triple-GEM, and PCB) was mounted in a stainless steel box that could be pumped down to 10^{-6} torr and was connected to the inlet and outlet gas lines to allow gas flushing. All measurements were done at atmospheric pressure with an overpressure of 0.5 torr in the detector vessel. The system contained also devices for the precise measurement of temperature, pressure and water content down to the ppm level. The ^{55}Fe X-ray source was positioned inside the box at a distance of $\sim$40 mm from the mesh. The total rate of X-rays was kept at the level of 1000 s^{-1}. 5.9 keV photons from ^{55}Fe release on the average 210 e in Ar/CO_2 (26 eV per electron-ion pair) and 110 e in CF_4 (54 eV per electron-ion pair) [19].

The discharge limit in the presence of heavily ionizing particles was studied with an ^{241}Am source that emits 5.5 MeV α-particles. The source in a container was attached directly to the drift mesh and strongly collimated in order to provide high energy deposition and small energy dispersion in the drift gap. The rate of the α-particles varied between $100 - 300$ s^{-1}. The distance between the active surface of the source and the drift mesh was $\sim$10 mm. The range of 5.5 MeV α-particles in Ar/CO_2 is $\sim$39 mm and about 18 mm in CF_4. Assuming perpendicular incidence of the α-particles to the drift gap, the energy deposition in a 3 mm gas layer is estimated to be $\sim$1.1 MeV for CF_4 and $\sim$0.30 MeV for Ar/CO_2,, producing $\sim$20,000 and $\sim$12,000 primary charges, respectively.

The beam test took place at KEK in May, 2004, with a 1 GeV/c secondary beam of negative particles (mainly pions) containing a few percent of electrons. The setup consisted of two gas Čerenkov counters (GCC), a set of scintillation counters (S1, S2 and S3), the HBD and a lead-glass calorimeter (PbGl). The HBD consisted of a 50 cm long radiator directly coupled to the detector box and setup described in Section 3. The detector was operated with pure CF_4 at a relatively high rate of 100 s^{-1}cm^{-2} and at a gain of $\sim$ 10^4. The trigger was defined by a coincidence between the three scintillation counters S1$\times$S2$\times$S3: S1 (100$\times$50 mm^2) was in front of the two GCC, S2 (25$\times$10 mm^2) just in front of the HBD and S3 (50$\times$45mm^2) was behind the HBD and in front of the PbGl. Pions were selected offline using the data from the two GCC, the PbGl and the time-of-flight measured between S3 and S1.

4.2 Gain in Ar/CO_2 and CF_4.

The gain as a function of the voltage across the GEM (ΔV_{GEM}) was measured with all GEMs at the same voltages for both Ar/CO_2 and pure CF_4. The absolute gas gain was determined from the measurements of the signal from ^{55}Fe 5.9 keV X-ray photons.

The gain was calculated using the measured relationship between the output signal from the amplifier and the input charge to a calibration capacitor and taking into account the average charge produced by one 5.9 keV photon (see previous section).

Fig. 6 shows the typical gain curves measured with 5.9 keV X-rays in Ar/CO_2 and CF_4 using small and large GEMs. Several detector sets were used and good reproducibility between the various sets was observed. Comparing the data for Ar/CO_2 and CF_4 in Fig. 6 one can see that the operational voltage for CF_4 is $\sim$140 V higher but the slopes of the gain-voltage characteristics are similar for both gases, i.e. an increase of 20 V in ΔV_{GEM}

causes an increase of the gain by a factor of ~ 3. The gain in CF_4 can reach values above 10^5, in spite of the very high operational voltage, as was already reported in [20].

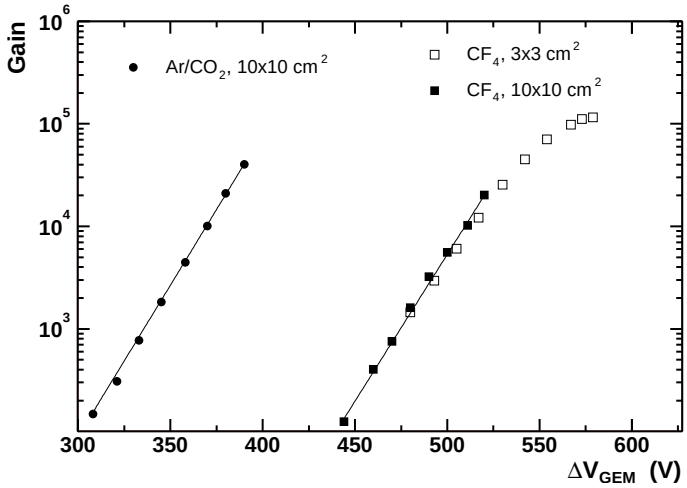

Figure 6: Gain as a function of GEM voltage measured with ^{55}Fe X-ray source. The 3×3 cm^2 detector had a CsI layer deposited on the top face of GEM1. The lines represent exponential fits to the data with 10×10 cm^2 GEMs.

4.3 Operation with the CsI Reflective Photocathode.

In all the tests with the CsI photocathode a mercury lamp was used for irradiation. In order to determine the total emission from the photocathode itself without any amplification in the GEMs, we applied a positive voltage between GEM1 and the mesh, thus collecting the emitted photo-electrons in the mesh.

The study of the triple GEM detector with a reflective photocathode was performed with $E_D = 0$ or slightly negative. Fig. 7 shows the current to the PCB as a function of the GEM voltage for the small GEM setup. The measurements were done in Ar/CO_2 and CF_4. In the CF_4 curve we can clearly see two regions well described by two exponential dependencies on ΔV_{GEM} (see lines in Fig. 7): an initial slow increase of current at lower voltages related to the increase of the extraction of the photo-electrons from the CsI surface into the holes of GEM1 and a steep exponential increase at higher voltages due to amplification in the GEMs.

In Ar/CO_2 these two regions are not so clearly separated because amplification in this mixture starts at lower voltages. The electron extraction cannot exceed the maximum level of 100% indicated by the dashed line in Fig. 7. Thus, the gain is determined as the ratio between the current to the PCB and the the extraction current. The latter is given by the first exponential curve up to $\Delta V_{GEM} = 350$ V and by the 100% extraction value at higher values of ΔV_{GEM}.

The gain as a function of ΔV_{GEM} for the setup with the reflective photocathode is shown in Fig. 8. In the same figure the data obtained with X-ray irradiation (^{55}Fe) are

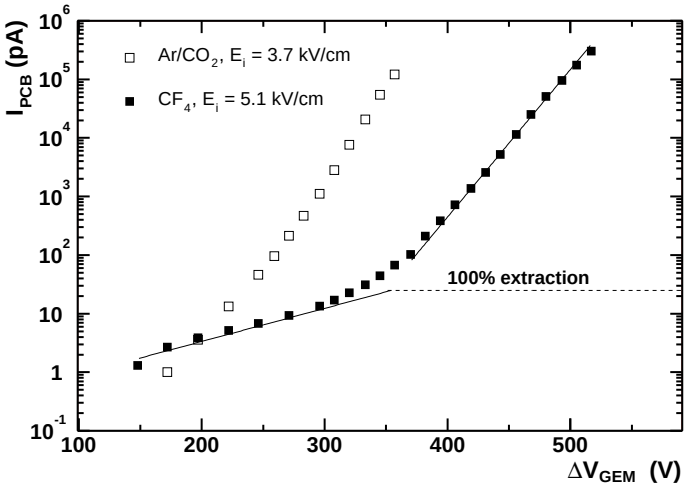

Figure 7: Current to the PCB as a function of ΔV_{GEM}.

also shown in order to demonstrate that the different methods of gain measurement give similar results.

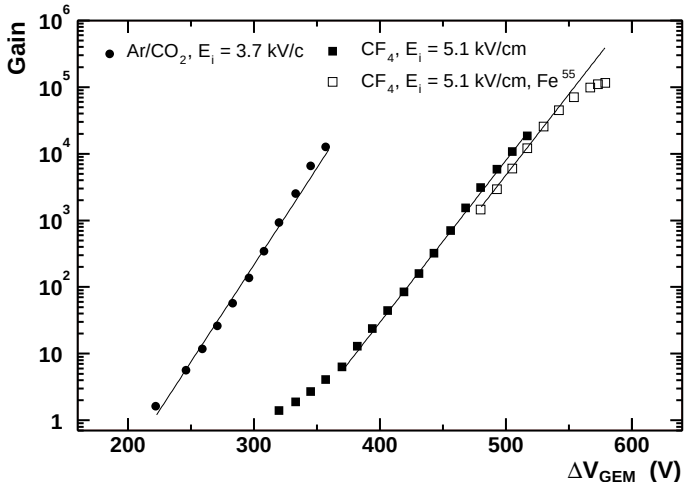

Figure 8: Gain as a function of ΔV_{GEM} for Ar/CO_2 and CF_4 measured with the UV lamp. For CF_4, the gain curve with ^{55}Fe is also shown. The lines are exponential fits to the data.

4.4 Discharge Probability and Saturation Effect.

Stability of operation and absence of discharges in the presence of heavily ionizing particles is crucial for the operation of the HBD. In our earlier paper [14] the discharge probability was measured in small GEMs while similar studies in large GEMs could not be done since any discharge destroyed the detector due to the large amount of energy stored in the large capacitance of the GEM. Measurements of the discharge limits in large GEMs were made

possible only when using HV-segmented GEMs and a triple-branch resistive chain. In the studies of discharge probability, the ^{241}Am source was used to simulate heavily ionizing particles under laboratory conditions.

An interesting feature of CF_4 which can already be seen in Fig. 6 is the strong deviation from exponential growth at high gains. This "non-linearity" is much more pronounced when the detector is irradiated with ^{241}Am α-particles as shown in Fig. 9. The figure shows the total charge in the avalanche measured with a pre-amplifier (dots). Since at high values of the charge, when the pre-amplifier is close to saturation, the output signal is already reduced compared to its real value, the measurements were repeated without any pre-amplifier, with the central pad directly connected to the 1 MΩ input of an oscilloscope through a 1 m coaxial cable. In this case the pulse height observed at the scope is determined by the ratio of the charge induced in the pad and the total capacitance of the pad including the capacitance of the cable. The measurements without pre-amplifier are also shown in Fig. 9. Both measurements were performed under identical conditions and for this purpose the pre-amplifier was calibrated in units of input charge. In order to obtain the relation between the signal measured without pre-amplifier and the input charge the results were normalized in the range ΔV_{GEM} = 420 - 440 V where both measurements could be performed and the pre-amplifier was still far from saturation. At $\Delta V_{GEM} > 490$ V the pulse-height resolution deteriorates considerably and we therefore plot the mean value (instead of the peak value) of the pulse-height distribution.

Fig. 9 shows clearly that the signal from alpha-particles deviates from the exponential dependence when the total charge in the avalanche exceeds the value of 10^7 electrons, leading to saturation when it reaches $\sim 4\times10^7$ e. (The saturation observed at 10^7 e is due to the saturation of the pre-amplifier).

This saturation effect is of prime importance for the anticipated application of the HBD in the PHENIX experiment where a small number of photoelectrons are to be detected in a high multiplicity environment of charged particles. It indicates that the total charge produced by a heavily ionizing particle is limited to below the Raether limit [21] and consequently its ability to provoke a discharge is strongly suppressed.

This suppression was observed in the measurements of the discharge limits performed with the segmented large triple-GEM detector. The results of these measurements are shown in Fig. 10. Two measurements are presented in the figure, the measurement in the presence of alpha-particles and the measurement without alpha-particles. In both cases the gain was monitored at each voltage with the ^{55}Fe source. The dependence of the gain on voltage is presented in the figure together with the spark frequency as a function of the GEM voltage. The duration of each measurement was $\sim$2000 s, i.e. the maximum number of sparks counted in the highest point was about 20. The present detector shows non-negligible spark probability at a gain $\geq 2\times10^4$. The results demonstrate that the discharge limit does not depend on the presence of alpha-particles in the sensitive volume of the detector. Rather it seems that only local defects in the GEMs can provoke discharges and limit the gain of the device.

During the series of tests the detector experienced a total number of 40 sparks but no sign of any degradation was observed in its performance and all three GEMs were still fully operational at the end of the tests.

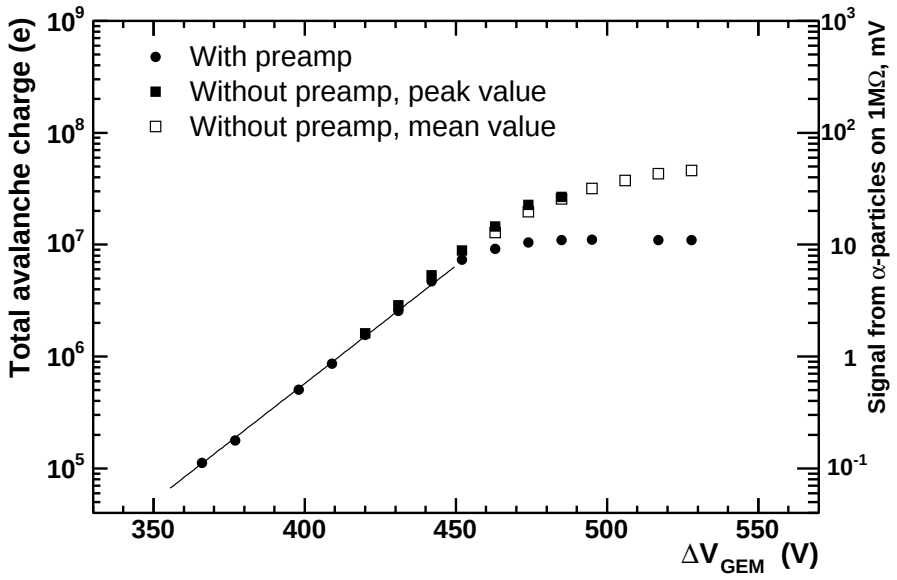

Figure 9: Pulse height of the signal from α-particles measured with and without the preamplifier as a function of GEM voltage. For the measurement with the preamplifier only mean values are plotted. For the measurement without the preamplifier both mean and most probable values are plotted (solid and open squares correspondingly).

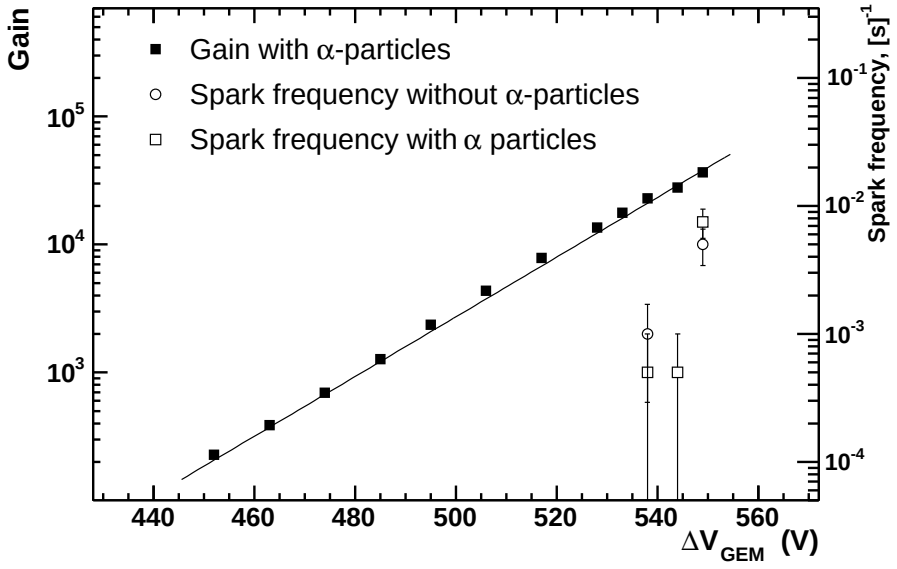

Figure 10: Spark frequency and detector gain as a function of voltage across GEM with and without α-particles irradiation.

4.5 Ion Back-flow in the Triple GEM Detector Operating with a Reflective Photocathode.

The flow of positive ions to the CsI layer is one of the potential damaging factors that can cause aging of the photocathode [18, 22, 23, 24]. We call this factor *ion back-flow* and

define it as the ratio between the current to the top electrode of GEM1 and the current to the PCB. This ratio depends on both the ion current itself and the fraction of electron current flowing to the PCB. This is a convenient definition as it allows us to estimate the actual ion current from the measured signal at the PCB.

In order to measure the current to the photocathode we supplied the voltage separately to the top electrode of GEM1 with a CAEN N126 power supply. The voltages to all other electrodes were supplied through the resistive chain.

In Fig. 11 the ratio of the current to the photocathode and the current to the PCB (ion back-flow factor) as a function of gain is shown for different conditions. The errors on the plots are mainly due to the limited accuracy of the photocathode current measurements. The value of the induction field was changed by changing the corresponding resistor in the chain and the value indicated in the caption (5.1 kV/cm) is reached at a gain of 10^4.

In Fig. 11a we see that in spite of the very different transport properties of the gases used in the measurements no significant dependence of the ion back-flow factor on the nature of the gas is observed as a function of gain and for different induction fields. The insensitivity of the ion back-flow factor to the particular gas at moderate gains is similar to that seen in [23]. It means that the efficiency of the transport of electrons and ions through the GEMs is the same for both gases and does not depend on diffusion.

The insensitivity of the ion back-flow factor to the electric field between the GEMs and in the GEM is demonstrated in Fig. 11b. Here the value of the ion back-flow factor as a function of gain is shown for three different electrostatic conditions: 1) standard, when the transfer field is equal to 3.4 kV/cm for both gaps and the induction field is equal to 5.1 kV/cm (the values refer to a gain of 10^4), 2) enhanced transfer field in both gaps, 3) reduced field in GEM1. From Fig. 11b we see that neither variation in electrostatic conditions between nor inside the GEMs affect significantly the ion back-flow factor.

The only parameter which affects the value of the ion back-flow in our case is the induction field. Fig. 11c shows the value of the ion back-flow factor as a function of the gain for 3 values of the induction field. The field in the induction gap does not affect the ion flow itself as ions are produced in the holes of the last GEM or in their vicinity, collected into the holes and then transported to the top gap. The only factor that is affected is the electron flow from GEM3 to the PCB. Thus the ion back-flow factor being higher than one at low induction field means that a fraction of the electrons is collected at the bottom face of GEM3 and consequently the amount of ions reaching the photocathode can be larger than the amount of electrons collected at the PCB. The increase of the induction field improves the electron collection efficiency at the PCB and reduces the value of the ion back-flow factor. It is clear from the figure that for E_I above 5 kV/cm the collection efficiency does not increase significantly resulting in a minimum value of the ion back-flow factor of ~ 0.7 at a gain of 10^4, consistent with results of [22].

During these measurements the photocathode was exposed to a total ion charge of $\sim$7 mC/cm^2. This charge density corresponds to $\sim$10 hours of continuous irradiation with $\sim 10^7$ photons/mm$^2\times$s at a gain of 10^4. In spite of this quite high ion back-flow the CsI quantum efficiency loss was not more than 30% after this irradiation.

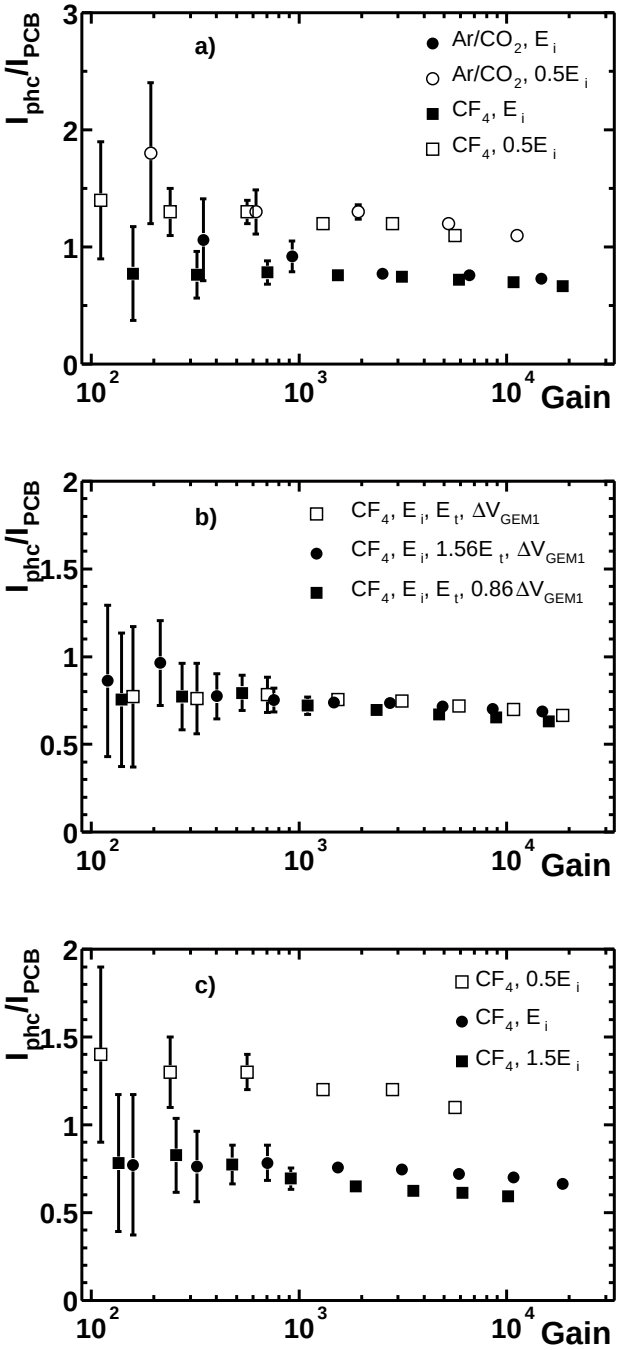

Figure 11: Ion back-flow factor as a function of gain. a) Comparison of ion back-flow factor for Ar/CO_2 and CF_4 and two different induction fields: standard E_I = 5.1 kV/cm and 0.5 E_I. The values refer to a gain of 10^4; b) Ion back-flow factor for different electrostatic conditions in the region between GEM1 and GEM3. c) Ion back-flow factor for 3 different values of the induction field.

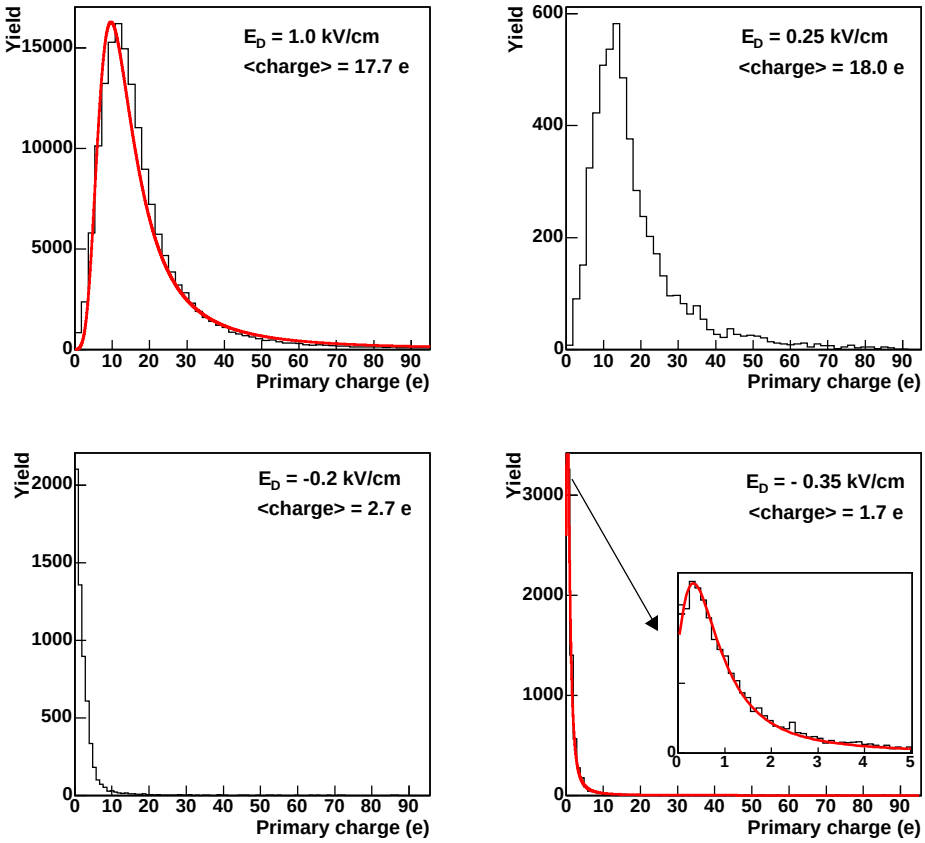

Figure 12: Pulse height spectra measured with 1 GeV/c pions at various values of the drift field E_D in the gap between the mesh and the upper GEM. The solid lines in the upper left and bottom right panels represent fits to Landau distributions of the measured spectra.

4.6 HBD Response to Mips and Photoelectrons

Fig. 12 shows the pulse height distribution, after pedestal subtraction, measured at KEK with 1 GeV/c pions for various values of E_D. The signal is expressed in terms of the primary ionization charge, using the ^{55}Fe spectrum measured under identical conditions. For $E_D = +1$kV/cm, the measured mean amplitude is $\sim$18 e corresponding to a primary ionization of 120 charges/cm or 54 eV/ion-pairs (assuming an energy loss of dE/dx = 7 keV/cm). The spectrum is well reproduced by a Landau distribution characteristic of the energy loss of a minimum ionizing particle (mip).

The spectrum remains practically unchanged as long as E_D is positive as shown for two cases in the upper panels of Fig. 12. As soon as E_D becomes negative there is a sharp drop in the pulse height as the primary charges get repelled towards the mesh. The mean amplitude drops to approximately 10% of its value for a positive field. The remaining amplitude results from the collection of ionization charges (i) from a thin layer above the first GEM surface and (ii) from the entire first transfer gap which are subject to a two-stage amplification. The mean amplitude vs. E_D is shown in Fig. 13. The figure shows

also the results of similar measurements performed with alpha particles. In both cases the results are practically identical. The amplitude decreases sharply when the polarity of the drift field is switched and this occurs within a ΔE_D range of $\sim$0.1 kV/cm.

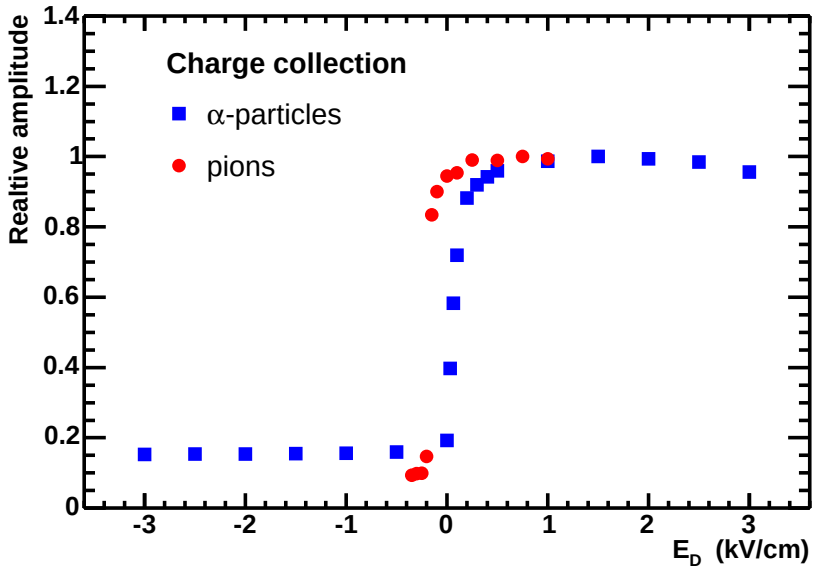

Figure 13: Collection of ionization charge vs. the drift field E_D in the gap between the mesh and the upper GEM.

The hadron rejection factor derived from the pion spectra measured at negative drift fields is shown in Fig. 14. The rejection is limited by the long Landau tail and depends on the amplitude threshold that can safely be applied without compromising the electron efficiency. Rejection factors of the order of 50 can be achieved with an amplitude threshold of $\sim$10 e. A much higher rejection factor is achieved by combining the amplitude response with the hit size. As already mentioned the pad readout consists of hexagonal pads with a size somewhat smaller than the blob size. Under these conditions charged particles will produce single-pad hits whereas electrons will almost exclusively produce multiple pad hits thereby providing an additional powerful handle on the charged particle rejection.

Similar measurements to determine the electron detection efficiency were performed with UV-photons from a Hg lamp irradiating the CsI photocathode through the UV-transparent CaF_2 window. We measured the current at the PCB for values of the HV accross the GEMs varying from 442 to 506 V and corresponding to a gas gain variation of more than a factor of $\sim$40. The results are shown in Fig. 15. The various measurements have been normalized to 1 at E_D=0 to represent the relative detection efficiency and to allow an easy comparison between the measurements. The relative detection efficiency is practically independent of the field across the GEMs. The current slightly increases as the positive drift field decreases, reaching a maximum at 0 kV. A mild decrease in the current is observed as the drift field becomes more and more negative demonstrating that the detection efficiency of the photoelectrons remains very high even at negative drift fields of 1kV/cm. Combining the results of Fig. 13 and 15 one sees that the best performance

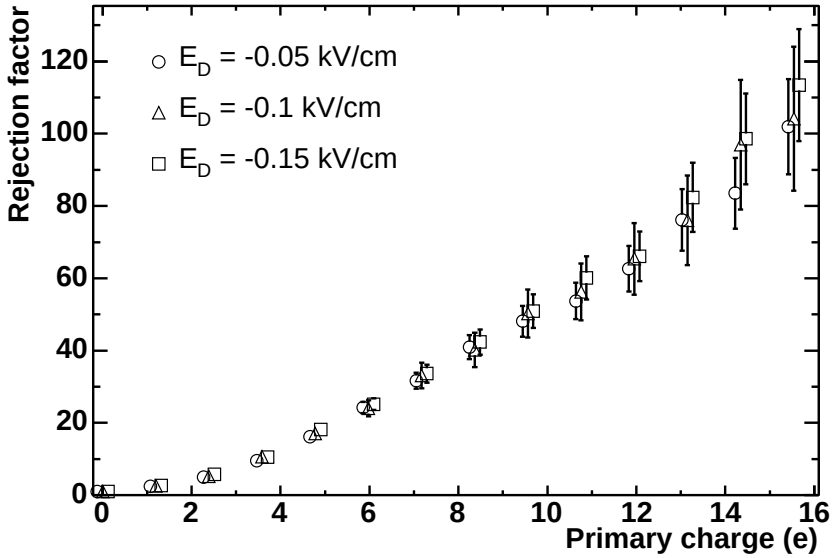

Figure 14: Hadron rejection factor derived from the pion pulse height distribution as a function of the amplitude threshold in units of the primary ionization charge. The errors bars represent the statistical uncertainties.

is achieved by applying a slightly negative field in the drift gap. The results presented here are consistent with those of Ref. [25].

4.7 CsI Quantum Efficiency

The absolute quantum efficiency (QE) of the CsI was measured by a large number of groups. (See [26]-[28] for a comprehensive review and further references). Most of the measurements are in reasonable agreement with each other. However, none of these measurements were performed at wavelengths below 150 nm (or photon energies above 8.3 eV). Since CF_4 is transparent up to 11.5 eV it was important to extend the measurements of the absolute QE of CsI as much as possible.

The determination of the absolute QE requires an absolutely calibrated light source, which is not available in most laboratories. Therefore, usually a relative method is used, namely recording of the sample response relative to a "known" reference. In our measurements we used as a reference a calibrated photomultiplier tube (PMT).

The experimental setup used for the determination of the absolute quantum efficiency of the CsI layer is shown in Fig. 16. It includes a vacuum ultraviolet (VUV) monochromator (H20, 115-500nm) equipped with a deuterium lamp (L7293, 115-320nm), coupled via a LiF window (cut-off at 105 nm) to a detector box. The monochromator box also includes a LiF beam splitter which splits the beam between photomultiplier PMT-0 and the detector box. PMT-0 serves as a normalization to monitor the deuterium lamp intensity. The detector box included an absolutely calibrated photomultiplier tube PMT (Hamamatsu R6836) on one side and on the other side a box containing a small (3×3 cm^2) GEM foil on which a 2500 Å layer of CsI was evaporated. Above the foil and at a distance of 1.5

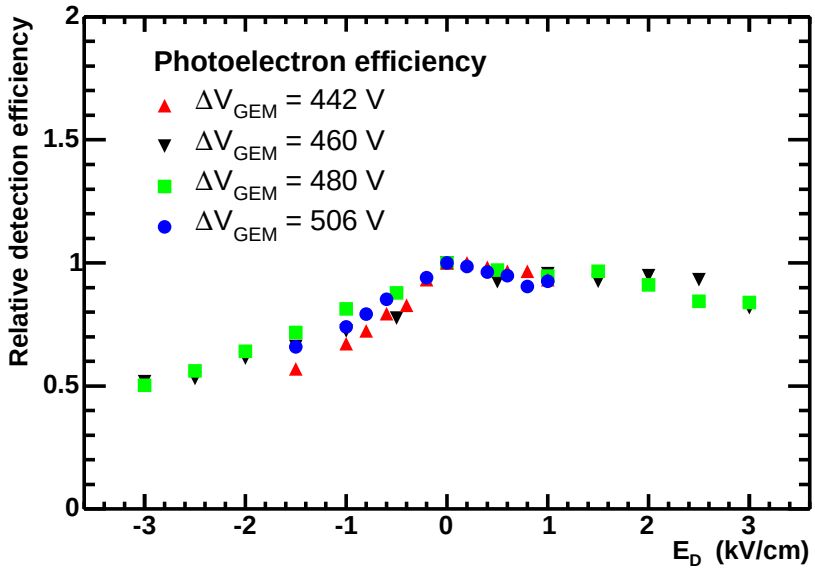

Figure 15: The photoelectron detection efficiencies at different gains vs. the electric field in the gap between the mesh and upper GEM.

mm from it was a mesh electrode which was at a positive voltage with respect to the foil. The detector box also had a UV mirror which served to deflect the beam alternatively to the CsI layer and to the PMT. Collimators of 8 mm diameter were placed in front of the mesh and PMT, making sure that the solid angle seen by the photomultiplier and the CsI layer were exactly the same. By rotating the UV-mirror the current was measured in turn over the whole wavelength range on both devices.

The current of the CsI and photomultiplier as measured in vacuum is shown in Fig. 17. The measurements were done over the wavelength range of 120 - 200 nm (E = 6.2 - 10.3 eV). The measurements were repeated with CF_4 at atmospheric pressure. The total path in CF_4 was 23 cm.

The absolute quantum efficiency of the CsI layer at a given wavelength λ is given by

$$(QE)_{CsI}(\lambda) = \frac{(QE)_{PMT}(\lambda) * I_{CsI}(\lambda)}{I_{PMT}(\lambda) * C_1 * C_2} \quad (1)$$

where $(QE)_{PMT}(\lambda)$ is the absolute quantum efficiency of the PMT at the wavelength λ, $I_{CsI}(\lambda)$ - the CsI photocathode current measured at that wavelength, I_{PMT} - the PMT photomultiplier current at λ , C_1 - the mesh transparency ($C_1 = 0.81$), and C_2 - the opacity of the CsI layer due to the GEM holes ($C_2 = 0.833$).

Fig. 18 shows the CsI absolute quantum efficiency in vacuum and CF_4 plotted as a function of the photon energy. (Plotting the quantum efficiency as a function of photon energy has the advantage that the figure of merit N_0 can easily be determined from the area under the points). The present results are in very good agreement with those of Ref [26] which covered the range 6-8.3 eV.

The range of the measurements shown in Figs. 17 and 18 (120 - 200 nm, or 6.2 - 10.3 eV) was limited by the light intensity of the deuterium UV lamp at ∼10.3 eV. Over

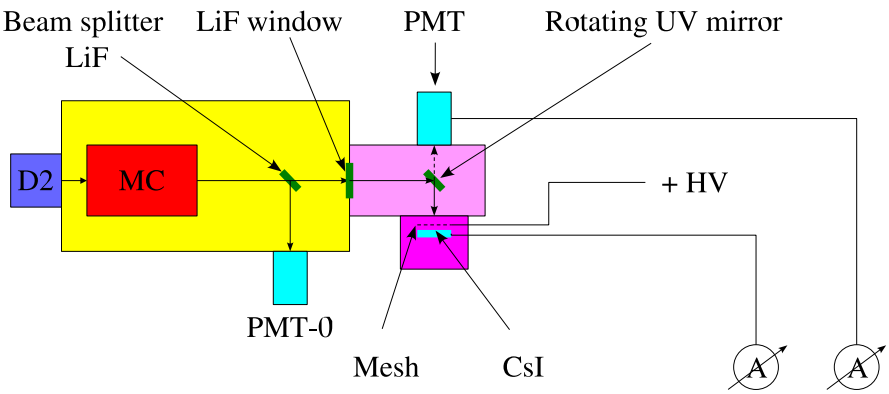

Figure 16: Schematic view of the experimental setup for measuring the quantum efficiency of the CsI layer.

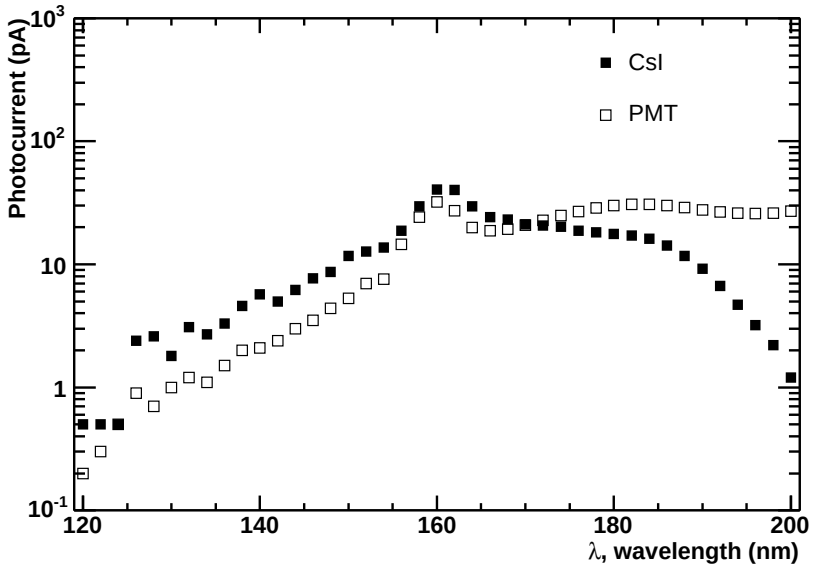

Figure 17: Photocurrent of CsI and PMT as function of wavelength.

this bandwidth we derive a figure of merit N_0 of 459 cm^{-1} (414 cm^{-1}) or an average QE value of 31% (28%) in vacuum (CF_4). However the useful range of UV photons in the HBD extends up to the CF_4 cut-off which is at 11.5 eV. Extrapolating the data of Fig. 18 to 11.5 eV under the assumption of a linear dependence of the quantum efficiency vs. photon energy gives a figure of merit N_0= 822 cm^{-1} or an average quantum efficiency of 55% in CF_4. For a 50 cm long radiator this N_0 value would correspond to ∼35 photo-electrons (pe) (after taking into account the losses due to the entrance mesh and the holes of the top GEM). A direct measurement of N_0 during the beam test at KEK was not possible due to the large UV absorption in the available gas system which was not of the required quality. We observed only 6-10 pe per electron trigger. This number is however consistent with the expected number of ∼35 pe after correcting it for the measured absorption in the gas.

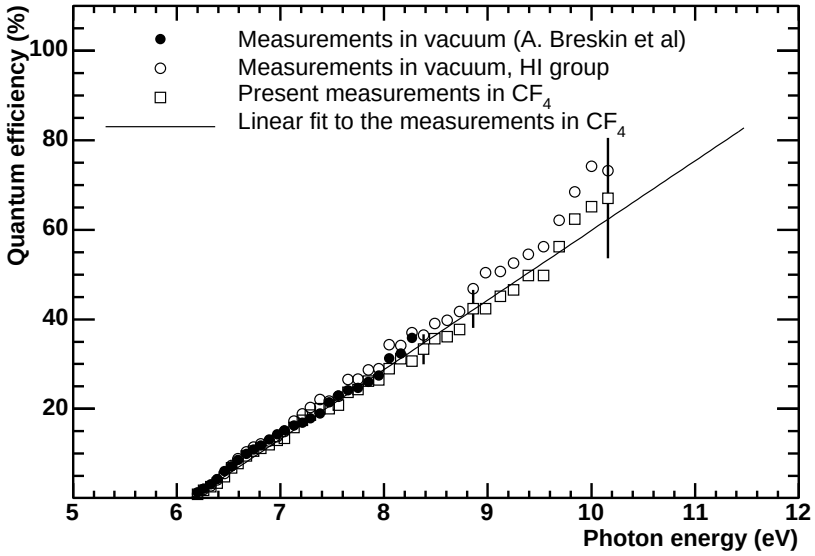

Figure 18: Absolute quantum efficiency of CsI in vacuum and CF_4 over the bandwidth 6.2 - 10.3 eV.

4.8 CF_4 Scintillation

CF_4 is known to scintillate. Its scintillation properties were studied by several groups with consistent results [29, 30]. The scintillation spectrum has a line at 163 nm and a continuum above 220 nm. Because of the latter, the HADES experiment abandoned the CF_4 option for their RICH radiator [29]. However, for the CsI photocathode which is sensitive only up to 200 nm this continuum is irrelevant. The CsI is sensitive to the line at 163 nm with a quantum efficiency of $\sim$25%. The strength of this line is 100-200 photons per MeV of deposited energy. Simple simulations [12] showed that the CF_4 scintillation will contribute a relatively small background uniformly distributed over the detector area. The measurements performed at KEK with a pion beam did not reveal any significant background in the test detector.

4.9 Aging Studies

In the present HBD two possible sources of detector degradation under irradiation can be identified: 1) Aging of the CsI photocathode due to ion back-flow and possible chemical reactions with active radicals formed in electron-ion avalanches in CF_4, and 2) aging of the GEMs due to etching of metal or insulator surfaces and/or polymerization of pollutants from avalanches in CF_4 at the metal or insulator surfaces. Both processes are determined by the total charge flowing through the detector which is the product of the photo-electron current collected into the holes of the first GEM and the total gain of the triple-GEM system.

Assuming a gain of $\sim 10^4$ in the detector we estimate conservatively the total charge flow through the HBD photo-detector to be 10-20 $\mu C/cm^2$/year. Thus the aging test of

the detector module should be performed up to an accumulated charge between 100 and 200 μC/cm^2 to represent several years of HBD operation.

The aging tests were performed so as to decouple the degradation of the photocathode from the deterioration of the GEMs. We used two sources of radiation: a UV Hg-lamp and an ^{55}Fe X-ray source. The UV lamp was used for continuous irradiation of the detector under test and the current to PCB was monitored. From time to time (once per 1-2 hours) the UV irradiation was stopped and the ^{55}Fe source was inserted into the detector for a short gain monitoring. During UV irradiation the electric field in the drift gap was kept at zero whereas during the X-ray irradiation the drift field was set to $\sim$1 kV/cm.

In Fig. 19 the results of two aging tests are shown. The first test (Fig. 19, left) was performed with a small triple-GEM detector. The test took about 1 day and the total charge accumulated was 140 μC/cm^2. Based on our estimate this charge corresponds to about 10 years of HBD operation. It is seen that the gain derived from the measurements of the current during UV-irradiation and the gain measured from ^{55}Fe irradiation are very close to each other. After an initial gain drop of $\sim$10% in the first 2 hours, the performance was stable within 2%.

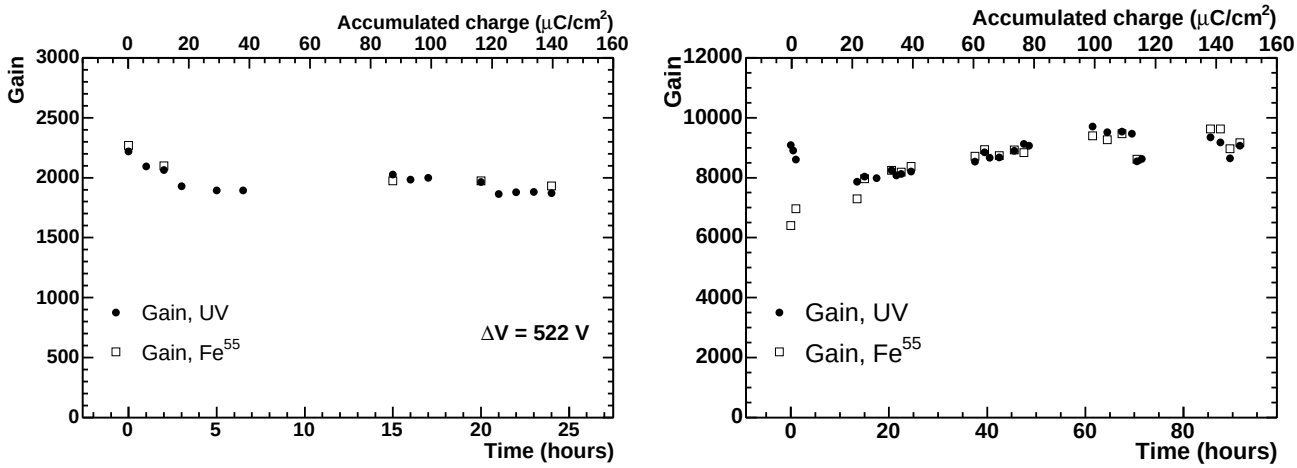

Figure 19: Results of aging tests with 3×3 cm^2 (a) and 10×10 cm^2 (b) 3GEM detector with CsI reflective photocathode. Open squares corresponds to the measurements with ^{55}Fe, solid squares represents the measurements with UV irradiation.

The second aging test was performed with a large segmented triple-GEM set. This test was done at a lower rate than the first one and the detector accumulated a total charge of $\sim$150 μC/cm^2 in 4 days (rather than in one day). As seen in the right panel of Fig. 19, the gain variations during the test did not exceed 20% and during the second half of the test they were even $\leq$ 5%. In the first 10 hours of the irradiation the gain derived from UV irradiation and the one determined from the measurements with ^{55}Fe source differed by $\sim$20%. This result indicates that the photocathode efficiency or collection efficiency of the photo-electrons into the first GEM holes was higher during that period. After the first 10 hours both gains converged to the same value and followed a very similar dependence. The performance of both small and large GEM sets during the initial phases of the aging tests including the gradual increase of the gain in the second test is not yet understood and will be the subject of further studies. However as a result of these tests

we conclude that both photocathode efficiency and GEM gain do not exibit any dramatic change which can be interpreted as degradation of the detector.

4.10 Test of a Triple GEM Detector in PHENIX

An investigation was recently carried out of a triple GEM detector operated during full luminosity Au+Au collisions within the PHENIX Central Spectrometer [16]. The detector was placed near the collision point, in an attempt to gauge its performance characteristics in a high multiplicity environment with respect to its performance in the lab. The GEM's were housed in a gas-tight vessel equipped with a thin mylar window to allow exposure to low energy background particles. The GEM's used were standard foils manufactured at CERN. They were 10×10 cm^2 in size, and had segmented electrodes in order to reduce the energy during a discharge. The detector was positioned within PHENIX in an orientation that closely resembles the final location of the proposed HBD, as illustrated in Fig. 20. The detector was mounted near the north central magnet pole tip with the mylar window facing the beam pipe at a distance of 50 cm. Pure CF_4 flowed through the vessel during the study while an ^{55}Fe radioactive source installed above the GEM's was used to monitor the gas gain. The signals from the GEM's, including those originating from the ^{55}Fe source, all particles produced from the heavy ion collisions, and any background, were all read out on a group of instrumented pads, comprising an effective area of $\sim 1.0 \times 1.5$ cm^2.

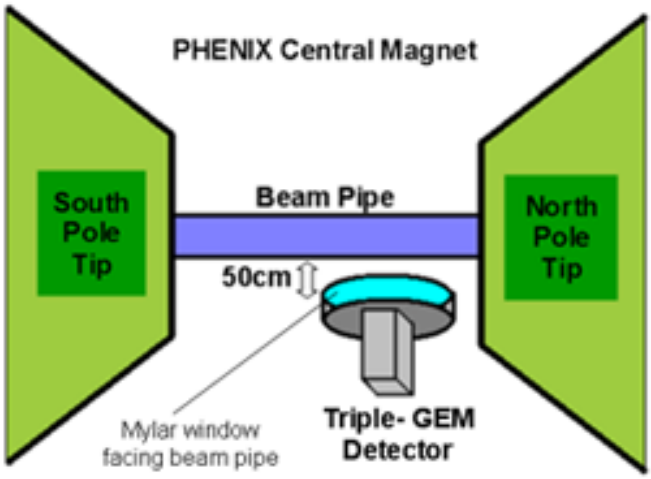

Figure 20: Triple-GEM detector mounted within the PHENIX Central Spectrometer. The detector is mounted such that its mylar window is at a distance of 50 cm from, and facing the beam pipe.

When the detector was first installed in PHENIX, a gain curve was produced as a function of the voltage applied across each foil with the beam off. The results were identical to those obtained in the lab, and confirmed that the detector was fully operational. The detector was then tested with the beam on at a gain of 3.3×10^3 in pure CF_4, and

gave an energy resolution of 38% FWHM for ^{55}Fe, similar to what it was in the lab. Overall, the detector easily passed the intended survival test, and operated smoothly at full RHIC luminosity, with no sparking or discharges observed over 24 hours of accumulated operation. In addition, the detector electronics were not adversely affected by the ambient magnetic field present during normal PHENIX operation, and the behavior of the detector was reproducible after exposure to the beam. As shown in Fig. 21, the gain and the energy resolution were both stable to within $\sim$ 10% at full luminosity throughout all the tests, as observed in the lab.

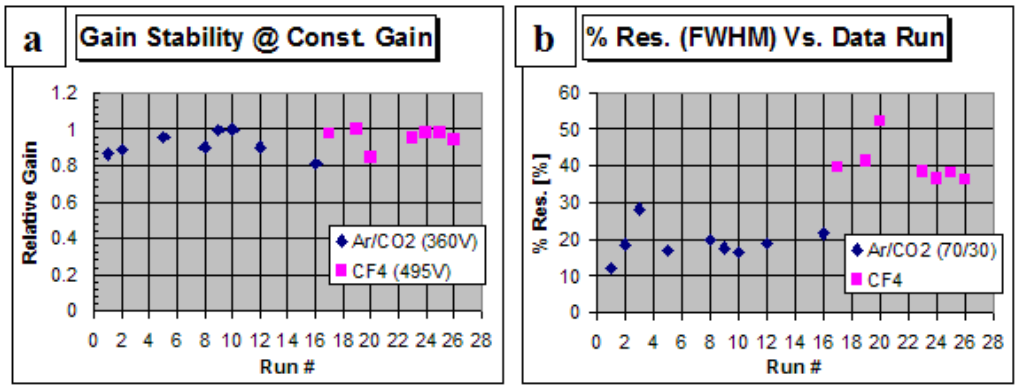

Figure 21: Plots of the relative gain (a) and FWHM % resolution (b) versus run number. The gain is constant to within $\sim$10% as expected from results in the lab, and the resolution is almost as consistent except for two points.

Although minimum ionizing particles were not recognizable due to the limited solid angle acceptance, the detector was sensitive to charged particles and other types of background. In self-triggered mode, a low energy peak was evident in the pulse height spectrum as depicted in Fig. 22. The level of this background grew as the detector was brought closer to the beam pipe. However, at 50 cm, the observed background level remained relatively low, and corresponded to a primary charge of less than $\sim$100 electrons (for comparison, we expected a primary charge of 94 electrons from mips.) When data was acquired in coincidence with beam-beam collisions, this background was negligible, where only 2.7% of the total hits recorded were above pedestal.

During the course of the study, the background levels in the self-triggered mode were observed to increase dramatically for a short period of time. The effect on the pulse height spectrum is shown in Fig. 22. In addition, in the beam-beam triggered mode, the number of hits recorded above pedestal rose to 5.1%. This behavior appeared to be due to poor beam conditions near the PHENIX collision point, which resulted in a large increase in beam related background. However, it appeared that most of this background was out of time with real beam-beam collisions, and resulted in a fairly small background in the beam-beam triggered data. Despite this period of high background level (which lasted only $\sim$15-20 minutes), the GEM continued to function properly afterwards. The fundamental implication of these tests is that the GEM detector worked reliably and was not overwhelmed with background in the central region of PHENIX corresponding to the proposed location of the HBD during full luminosity Au+Au collisions.

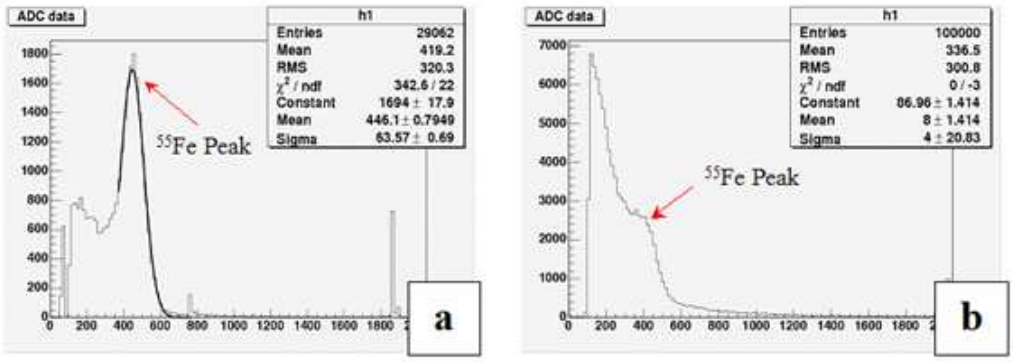

Figure 22: Triple GEM ^{55}Fe pulse height spectrum taken inside the PHENIX Central Magnet at full RHIC luminosity. a) During normal operation, the self-triggered background levels are relatively low. b) During a period of high background, believed to be due to poor beam conditions.

5 Mechanical Design of the Final HBD

The mechanical design has been developed and construction procedures have been practiced over the past few months. The design derives from the system specifications discussed in Section 3 and the space constraints. In addition, special care is taken to minimize (i) the amount of material in order to reduce as much as possible the amount of conversions in the central arm acceptance and (ii) the dead or inactive areas due to frames or spacing between adjacent detector modules in order to achieve the highest possible efficiency. A full scale prototype has been designed (detailed drawings are available at: *https* : *//www.phenix.bnl.gov/phenix/WWW/p/draft/ravini/hbd_drawings/prototype*) and appropriate tooling and jigs have been designed and constructed. At present the construction of the prototype is almost complete.

This section describes the mechanical design and construction procedures of the final HBD. The design is very similar to the full scale prototype. The main difference is that the acceptance has been enlarged to allow operation of the HBD both in its nominal position (starting at r= 5 cm) and in a retracted position (starting at r=22 cm). Table 1 summarizes the most important design parameters.

Table 1: Design parameters of the HBD.

Acceptance nominal location (r=5 cm)	$\|\eta\| \leq 0.45$ $\Delta\phi$ =135^o
retracted location (r=22 cm)	$\|\eta\| \leq 0.36$ $\Delta\phi$ =110^o
GEM size ($\phi \times z$)	23 × 27 cm^2
Frame	5 mm width, 0.3mm thick cross
Hexagonal pad size	a = 15.6 mm
Number of pads per arm	1152
Dead area within central arm acceptance	6%
Radiation length within central arm acceptance	1.46%
Weight per arm (including HV and gas connectors)	<10 kg

The HBD is made of two identical arms, located close to the interaction vertex. In most measurements of low-mass electron pairs, the silicon vertex detector is not installed and the HBD location starts right after the beam pipe at r$\sim$5 cm and ends at r$\sim$60 cm (see Fig. 4 and Fig. 23). In this configuration, each arm covers 135^o in azimuth (ϕ) and $\pm$0.45 units of pseudorapidity (η). This extended acceptance with respect to the central arms provides a very generous veto area for efficient rejection of close pairs (see Appendix). For low-multiplicity measurements, as for example in p+p and p(d)+Au collisions, the HBD can work in conjunction with the silicon detector, in which case the HBD location starts at r$\sim$22 cm. The acceptance in this retracted position is also indicated in Table 1.

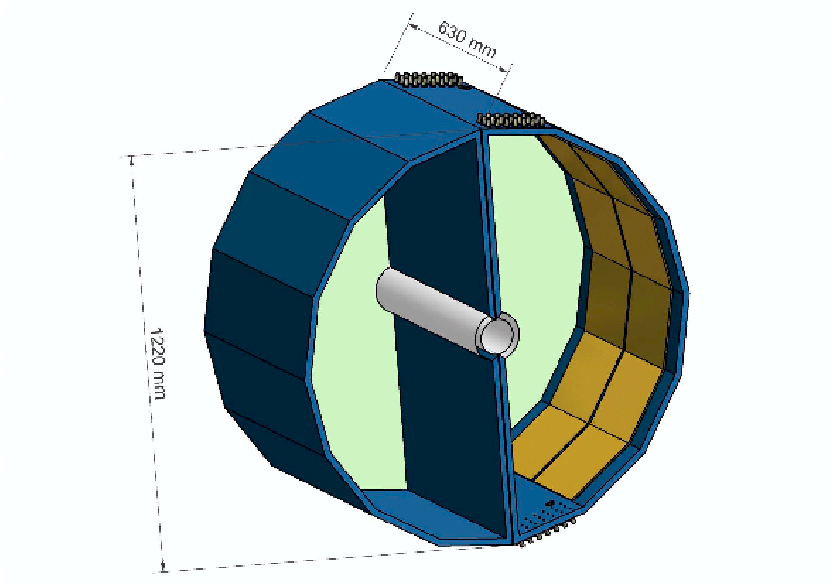

Figure 23: 3-d view of the HBD final design

Each arm consists of a $\sim$50 cm long radiator directly coupled to a triple GEM photon detector. The latter is subdivided in 12 detector modules, 6 along the ϕ axis $\times$ 2 along the z axis (see Fig. 23). With this segmentation, each detector module is $\sim$ 23$\times$ 27 cm^2 in size. Fig. 24 presents an exploded view of the back-side of the HBD, showing the various components of one detector module and the vessel envelope to which it is attached. The entrance mesh and the three GEM foils are mounted on FR4 fiberglass frames. The frames have a width of 5 mm and a thickness of 1.5 mm that defines the intergap distance. To prevent sagitta of the foils in the electrostatic fields, the frames have a supporting cross shape (0.3 mm thick) in the middle. The three GEM foils and the mesh are stacked together and attached to the detector vessel by 8 pins (located at the corners and the middle of the frame) which also allow stretching them and maintaining a minimum deformation of the 5 mm wide frames. Special tooling has been developed to stretch the foils and the mesh and glue them onto the narrow frames. The design allows for only 1 mm clearance between two adjacent detectors. With this design, the resulting total dead area within the central arm acceptance is calculated to be 6%.

The detector anode is a double-sided printed circuit board (PCB) with the hexagonal pad pattern on the inner side and short ($\sim$1.5 cm long) signal traces on the other side.

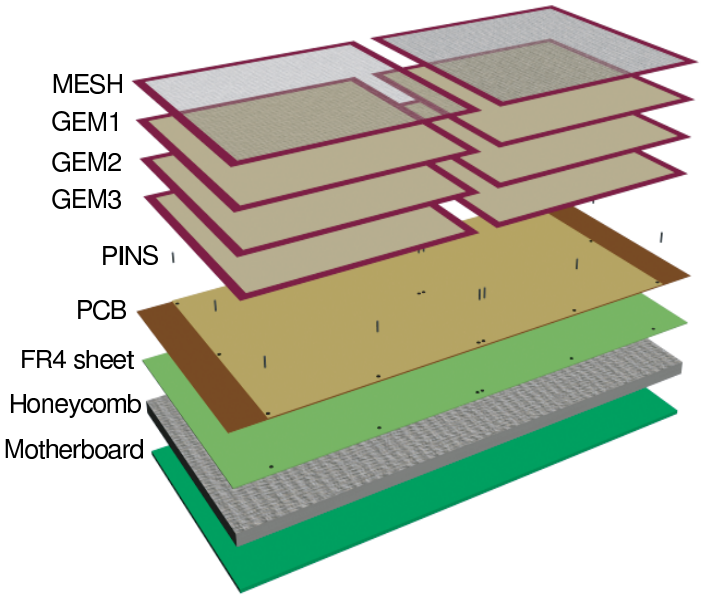

Figure 24: Exploded view of a panel of the HBD

Plated-through holes in the PCB connect the pads to the traces. With a hexagon side of a = 15.6 mm there are a total of 1152 pads in each arm. The PCB is made of 50 μm thick Kapton foil with 5 μm copper cladding, in one single piece (∼140 x 63 cm^2).

The detector vessel has a polygonal shape formed by panels glued together as shown in Fig. 23. The PCB is glued to the six panels which are behind the HBD active area. These panels consist of a 0.25 mm thick FR4 sheet and a 0.5 mm multilayer motherboard glued to a 19 mm thick honeycomb core. Short wires are soldered at the edges of the signal traces and passed through small holes in the panels to bring the pad signals to the outer side of the motherboard into which the individual preamplifiers are plugged (see Fig. 25). The other panels, outside the active area, are made of honeycomb sandwiched

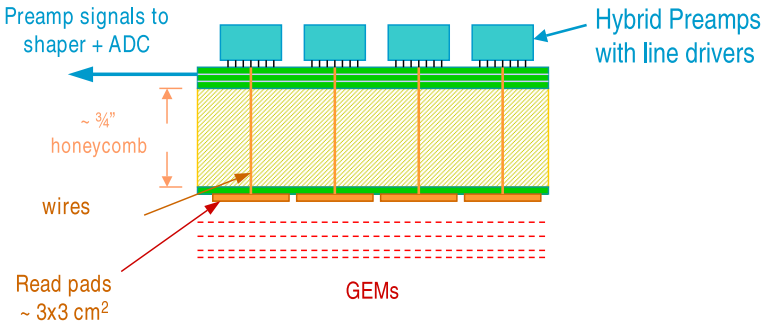

Figure 25: Backplane of detector panel consisting of hexagonal pad plane connected by wires to the readout board containing the preamps.

between two 0.25 mm thick FR4 facesheets. An FR4 frame, 19 mm wide and 7 mm thick connects all panels together on each side providing mechanical stability and rigidity to the entire box. The two sides of the box are closed with covers (also made of honeycomb

Table 2: HBD radiation budget within the PHENIX central arm acceptance.

Component	Material	X_0 (cm)	Thickness (cm)	Area (%)	Rad. Length (%)
Window	Mylar	28.7	0.005×2	100	0.035
Mesh	SS	1.67	0.003	8	0.014
GEM	Kapton	28.6	0.005×3	64	0.034
GEM	Copper	1.43	0.0005×3	64	0.067
GEM frames	FR4	17.1	0.15×4	6.5	0.228
PCB	Kapton	28.6	0.005	100	0.017
PCB	Copper	1.43	0.0005	80	0.028
Facesheet	FR4	17.1	0.025	100	0.146
Panel core	Honeycomb	8170	1.905	100	0.023
Mother-board	FR4	17.1	0.05	100	0.292
Mother-board	Copper	1.43	0.0005	100	0.035
Total					**0.92**
Gas	CF_4	9240	50	100	**0.54**

sandwiched between two 0.25 mm thick FR4 facesheets) which are bolted on the frame with an 0-ring seal. Gas-in and gas-out connections and HV connectors serving the GEMs are located on the top and bottom panels.

Special attention was taken in the design to ensure tightness of the box once closed. The plated-through holes are effectively sealed by the panels glued on the back side. Making the PCB in one piece and glueing it to the panels behind it solves the problem of potential leaks at the junctions between these panels. The other junctions are easily sealed by glueing a 50 μm thick mylar stripe along the inner side of the junction. A double mylar window (2×50 μm thick) is glued onto the vertical panels (close to the beam axis) to further reduce the radiation length in the HBD fiducial acceptance. Provision is made to have N_2 gas flowing in the space between the two mylar foils to prevent water vapor diffusion into the detector.

With this design each box weighs ∼5 kg. Adding all accessories (HV connectors, gas in/out, GEM foils, preamplifier cards...) results in a total weight of less than 10 kg per arm. The total radiation length within the central arm acceptance is calculated to be 0.919%. The radiation budget is itemized in Table 2. To this, one has to add the contribution of the 50 cm CF_4 gas which amounts to 0.541% of a radiation length.

6 Monte Carlo Simulation and System Performance of the Prototype

The HBD full scale prototype has been integrated into the PHENIX standard simulation package (PISA). A 3-d view of the prototype is shown in Fig. 26. As mentioned in the previous section, the main difference compared to the final design is the smaller acceptance. As a consequence, the GEM size, the pad size and the number of detector

modules are different. Table 3 lists the differences between the full-scale prototype and the final design. Since in the latter the veto area is larger and the pad size is smaller, the Monte Carlo simulation results presented in this section are expected to be slightly better for the final HBD.

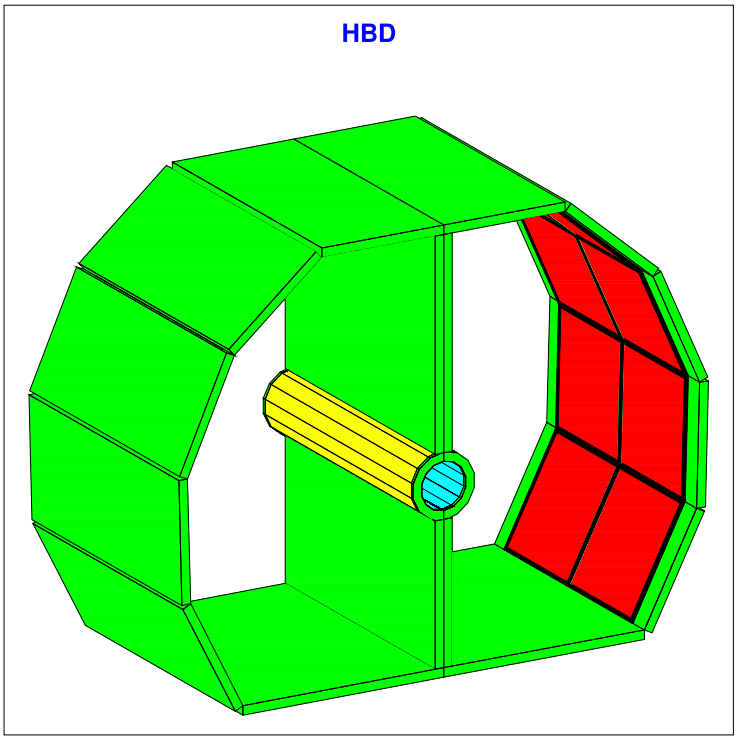

Figure 26: 3-d view of the HBD full scale prototype.

Table 3: Main differences in the design parameters of the final and full scale prototype detectors.

	Final HBD	Full scale prototype
Acceptance	$\|\eta\| \leq 0.45$ $\Delta\phi$ =135^o	$\|\eta\| \leq 0.4$ $\Delta\phi$ =100^o
Number of detector modules	24	16
Number of pads per arm	1152	684
GEM size ($\phi \times z$)	23 × 27 cm^2	26 × 24 cm^2
Hexagonal pad size	a = 15.6 mm	a = 16.7 mm

6.1 PISA Input Parameters.

- Geometry
  The simulations were performed using the full-scale prototype geometry. The HBD

inner radius is R = 5 cm and the outer radius is R = 60 cm. Each arm covers 100^o in the azimuthal direction (ϕ) and $\pm$ 0.4 units in pseudorapidity (η). There are eight identical detector modules per arm (2 along the Z direction $\times$ 4 in the azimuthal direction). Each detector module has an active area of approximately 26x 24 cm^2.

- Materials The prototype is built out of panels made of honeycomb (3/4" thickness) covered with FR4 (0.25 mm thick) plates on each side. The whole structure is supported by a 7 mm thick FR4 frame. The entrance to the HBD is a double mylar (2$*$0.05 mm thickness) window flushed with nitrogen. The width of the GEM supporting frames (FR4) is 5 mm.

- Absolute quantum efficiency
  The results of our measurements of the CsI absolute quantum efficiency in the energy range 6 - 10.3 (see Section 4.7) extrapolated to 11.5 eV (CF_4 cut-off) with the assumption of a linear dependence are used in the present HBD simulations.

- Gas gain
  In the simulations the detector is operated at a gain of 10^4.

- Response to hadrons
  The signal measured in the beam test at KEK with 1 GeV/c pions under reversed drift field conditions is used to simulate the dE/dx response of hadrons (see Fig.12).

- Pad size
  The detector anode plane is a printed circuit board with hexagonal pads of side a = 1.67 cm resulting in a total number of 1368 channels. A pad amplitude threshold of 1 p.e. (i.e. a charge of 1.6 fC at a gas gain of 10^4) is assumed in the simulations.

- Magnetic field
  All simulations presented here where performed with the compensated +- configuration of the magnetic field.

6.2 HBD Pattern Recognition and Single Particle Response

The HBD pattern recognition algorithm and tracking have been implemented into the PHENIX reconstruction software in the Fun4All framework. We first studied the detector response to single particles. Single electrons at several momenta and single mips were generated. Hits of particles traversing the HBD are reconstructed using a cluster algorithm. A cluster is defined as a group of adjacent fired pads where a fired pad implies a pad signal above a threshold of 1.6 fC. In order to cope with overlapping hits a simple cluster splitting algorithm is implemented: if the reconstructed cluster has more than one local maximum the algorithm divides it into subclusters and the amplitude of the pads between the two maxima is shared between the subclusters in proportion to the maxima. The center of gravity of the isolated clusters is taken as the hit position of the incident particle. The amplitude distribution of single electrons in units of fC is shown in Fig. 27 by the blue points. The mean amplitude is approximately 58 fC. This charge corresponds to $\sim$36 photoelectrons per primary electron at a gas gain of 10^4 and it is very close to

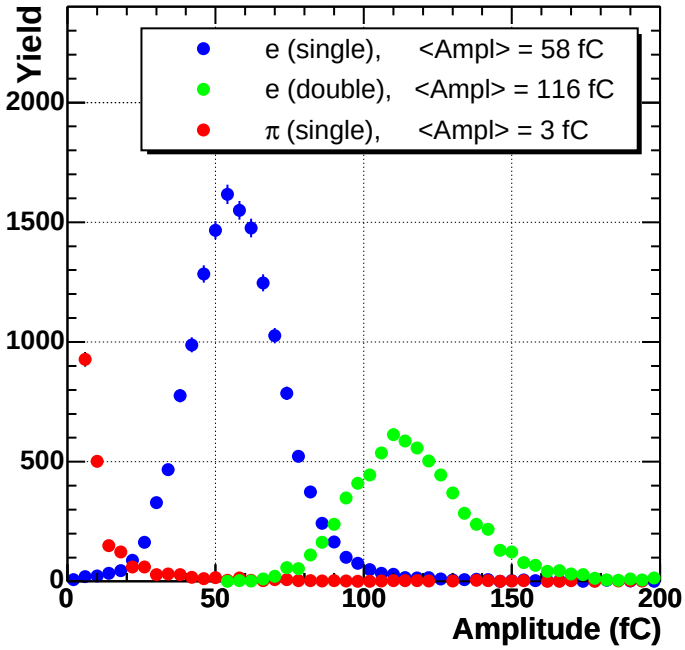

Figure 27: Pulse height distribution calibrated in fC for single electrons (blue points), double electrons (green) and for pions (red points).

the expected value given the input parameters. The response to pions is also shown in Fig. 27 by the red points. Since a much higher hadron rejection factor can be achieved by combining the amplitude response with the hit size we show in Fig. 28 the number of fired pads per electron hit and per pion. The results show that for electrons, the probability of single pad hit is only 3.1% while for pions this probability is practically 100%.

Based on the results shown in Fig. 27 and in Fig. 28 the hit is defined as an electron hit if the cluster amplitude is greater than 32 fC (20 pe) and the number of fired pads in the cluster is larger than one ($N_{pads} > 1$). With this definition the electron detection efficiency in the HBD is 92.2% for p >50 MeV/c as shown in Fig. 29. The efficiency losses are mainly due to the thresholds in the amplitude and size of the cluster and they occur close to the dead areas of the detector. It will be possible to recuperate some of these losses by using a cluster amplitude threshold which varies across the detector area taking into account the dead areas.

6.3 Tracking

Electrons in the central arms are reconstructed with the RICH and EMCal using the standard cuts (track quality 31 or 63, n0≥3, disp ≤5, chi2/npe0 ≤10, 0.7 < E/p < 1.3). These electrons are then tracked to the HBD with 3σ momentum dependent matching cuts both in Z and ϕ.

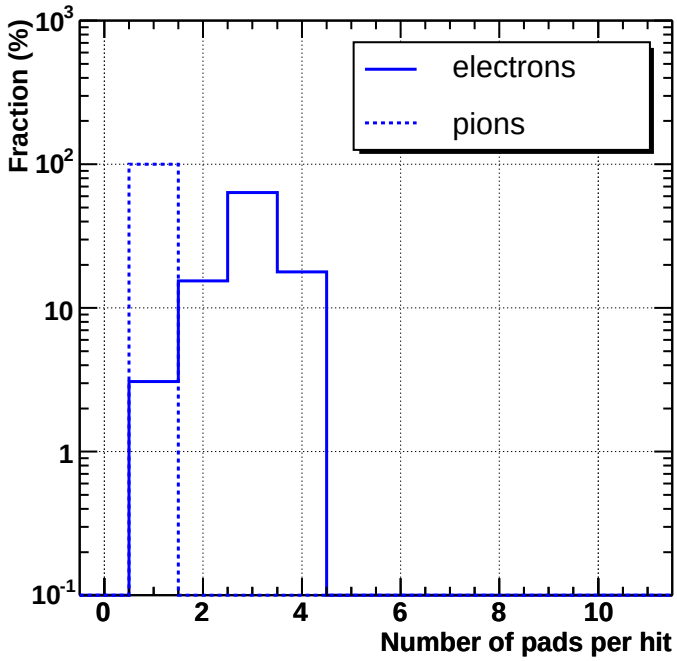

Figure 28: Number of fired pads per electron hit.

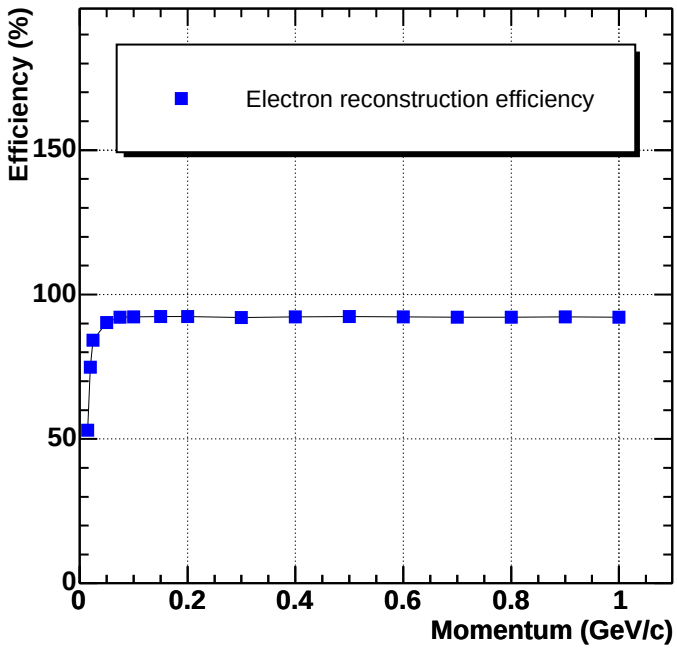

Figure 29: Single electron detection efficiency in the HBD as function of momentum

6.4 Au+Au Events Generation.

6.4.1 Central HIJING Events.

In order to study the HBD ability to reject the combinatorial background 73K central HIJING events were generated, passed through PISA in the compensated magnetic field

configuration keeping all necessary information for the electron analysis in the Central rms and then were reconstructed. We chose a very narrow centrality window: impact parameter b < 2 fm (top 2%) which corresponds to an average charged particle rapidity density of $dN_{ch}/dy = 940$. The events were generated at the vertex z = 0 cm. We plan to run another set of the HIJING events with a different vertex position (Z = 25 cm).

6.4.2 Event Display

A single central HIJING event is shown in Fig. 30: the left panel shows the PISA (GEANT) hit positions of all hadrons (small blue dots), electrons (yellow circles) and positrons (red circles) crossing the HBD pad plane. The right panel shows the reconstructed electron clusters in the same event. Out of the huge number of charged particles going through the HBD only two are seen in the detector. The excellent hadron rejection is achieved for two reasons: (i) the signal produced by hadrons is below the pad threshold or (ii) the hit did not pass the amplitude or size cluster cut. The two hadron hits seen in the reconstruction pass the cluster cuts by pile-up of hadron hits in these very high multiplicity events. The average number of charged particles traversing the HBD in these central HIJING events is ∼400. The average number of fired pads (in a raw event, after applying the pad threshold) is 211 which corresponds to a pad occupancy of about 15%. There are a large number of electron and positron hits in the HBD as seen in the left panel of Fig. 30. Many of them (electrons with momentum below the Čerenkov threshold, electrons reentering the HBD after reflection in the magnetic field, electrons not coming from the vertex) do not lead to a reconstructed signal. There are on the average 19 reconstructed electrons per event, 5.7 originating from the vertex and 13.5 not originating from the vertex (mainly from the nose cones).

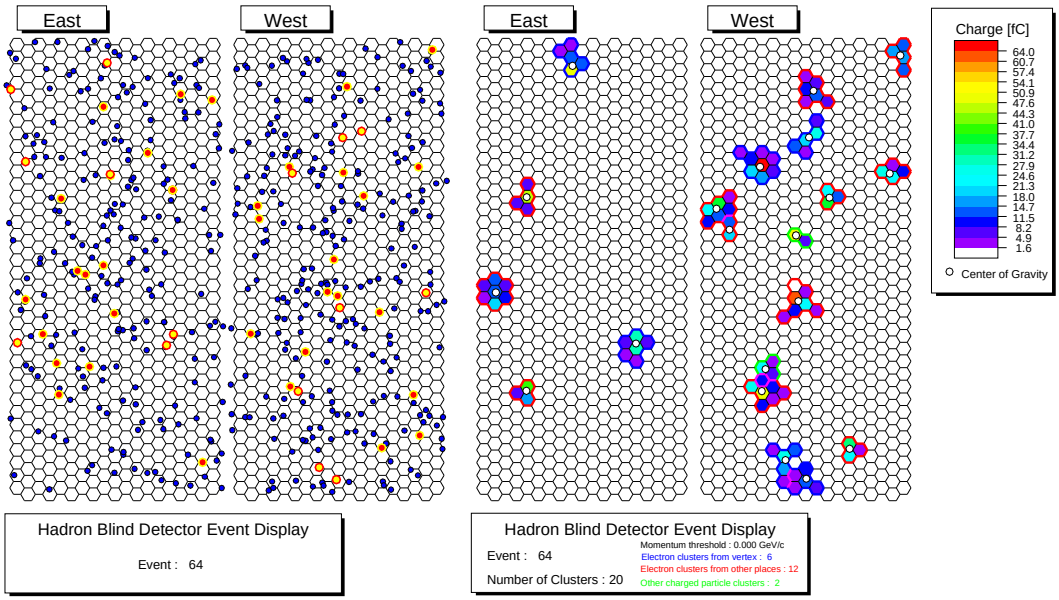

Figure 30: HBD event display of a central HIJING event (see explanation in the text).

6.4.3 Central HIJING Events Merged with $\phi \rightarrow e^+e^-$

In order to study the signal efficiency in the HBD as well as the expected improvement of the S/B ratio, each HIJING event was merged with a single $\phi \rightarrow e^+e^-$ event generated in the Central Arm acceptance. These merged events were then passed through PISA and the reconstruction chain, in exactly the same way and using the same cuts that were applied to the pure HIJING events.

6.5 Combinatorial Background Rejection

The rejection of the combinatorial background is done in several steps which are shown in Fig. 31: in the first step (top left panel) the electrons and positrons detected in the Central Arms are used to construct the e^+e^- invariant mass spectrum. This plot represents the current status of the dielectron combinatorial background in the existing PHENIX setup without the HBD. In the second step (top right panel) the electrons reconstructed in the

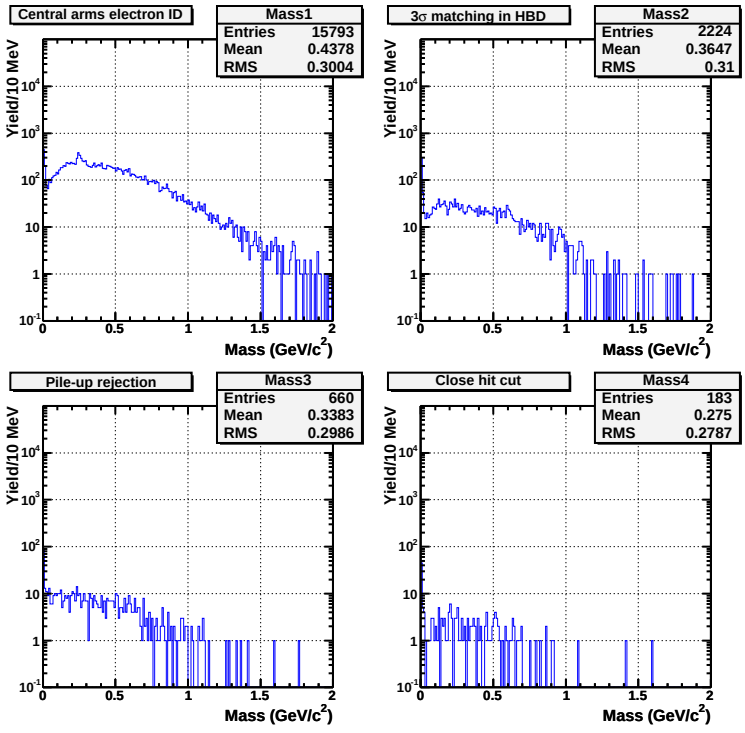

Figure 31: The combinatorial background (see explanation in the text).

Central Arms are matched to the HBD. As was stated above, 3σ momentum dependent matching cuts, both in z and in ϕ, were used in the tracking. This matching reduces the combinatorial background by a factor of $\sim$7 which is mainly due to electrons which are not seen by the HBD but were bent into the Central Arms by the magnetic field or to electrons produced outside of the HBD acceptance. In the third step (bottom left panel) the clusters with amplitude $>$ 96 fC ($\sim$60 p.e.) are rejected. These double amplitude clusters are mainly originating from γ conversions. With this step we gained an additional rejection factor of $\sim$3. The bottom right panel is the last step: here the

electron tracks which have another electron in the HBD within a distance of 200 mrad (close hit cut) are removed. With this final cut the combinatorial background is reduced by an additional factor of ∼4 and the overall rejection factor averaged over the whole mass region ($0 \div 2$ GeV/c^2) is close to 90.

Fig. 32 (blue points) shows the rejection factor versus dilepton mass in five mass regions which are indicated on the plot. In order to test the sensitivity of the results to possible losses, we also performed simulations in which the quantum efficiency was

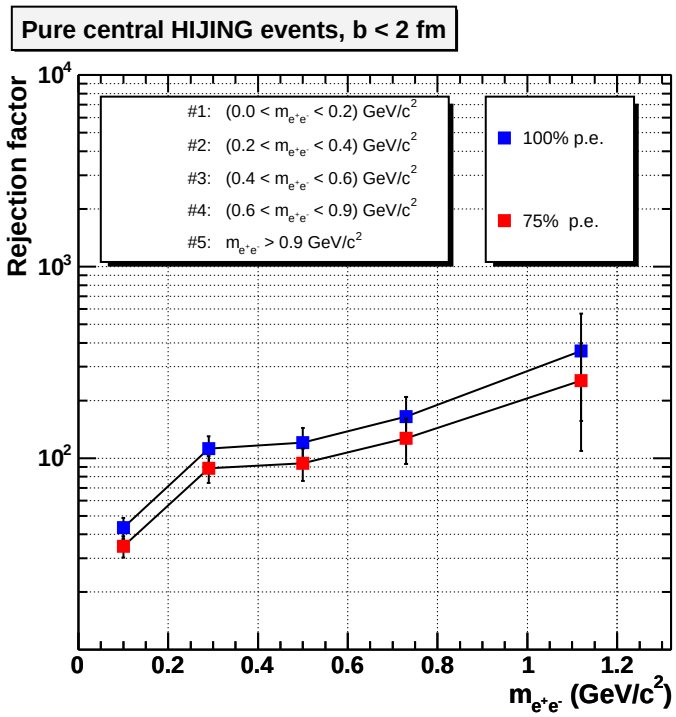

Figure 32: Rejection factor as a function of the dilepton mass: the blue points are for the nominal number of p.e. (36), the red points represents a reduced number of p.e. (75%)

reduced by 25%. The results are shown in fig. 32 by the red points. The rejection factors are somewhat smaller but still large enough. As it will be shown below, at these levels of rejection, the quality of the low-mass pair measurement will not be limited anymore by the combinatorial background produced by γ conversions and π^0 Dalitz decays but rather by the combinatorial background from the semileptonic decays of charmed mesons.

6.6 Signal Efficiency

The results of the reconstruction of HIJING events merged with a $\phi \rightarrow e^+e^-$ signal using the same rejection steps as explained in the previous section are shown in Fig. 33. The combinatorial background in these merged events is much higher than for pure HIJING events. This is due to the fact that in every event there are two additional electrons coming from $\phi \rightarrow e^+e^-$ decay, which is not a realistic case. The number of ϕ mesons (signal) was calculated for the mass window $0.98 < m_{e^+e^-} < 1.05$ after subtracting the background events. The number of background events was roughly estimated by taking

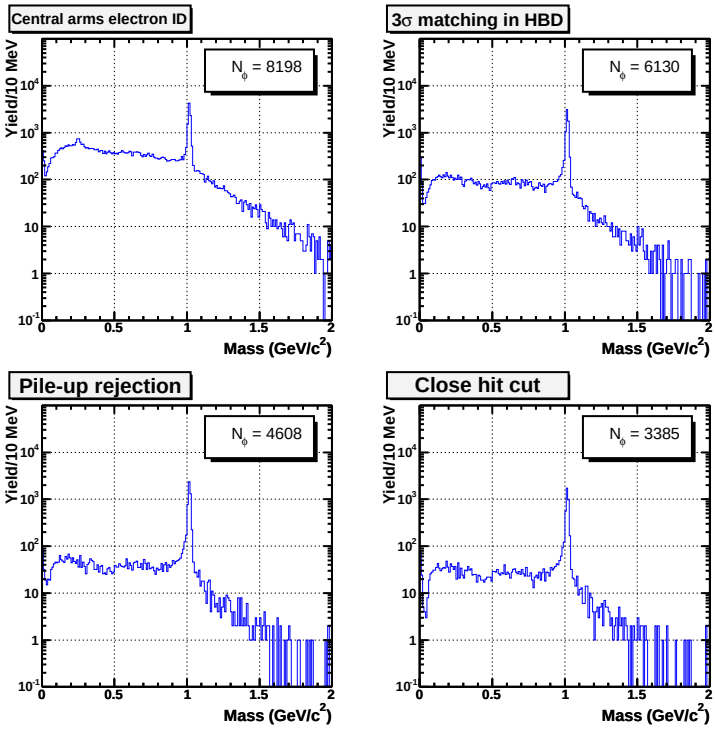

Figure 33: The signal evaluation (see explanation in the text).

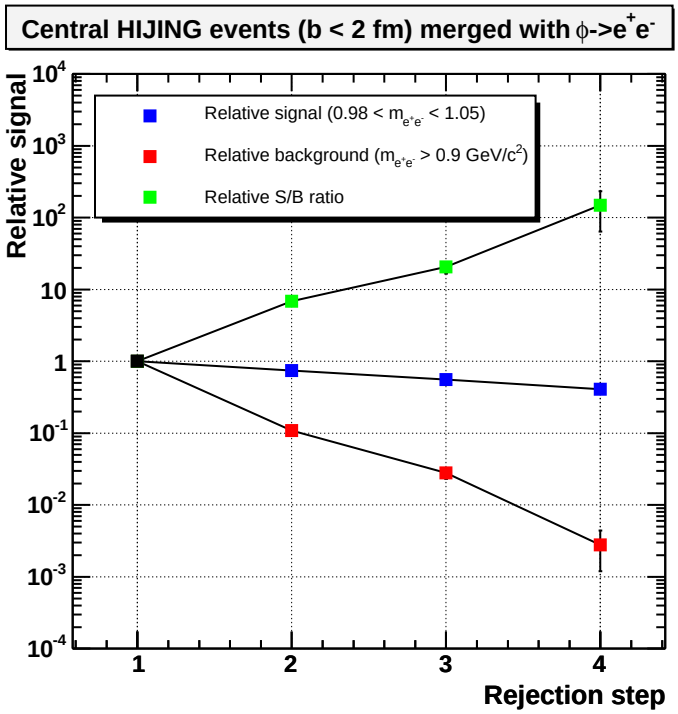

Figure 34: Relative signal, backgropund and S/B ratio as function of rejection steps.

the average between the first and the last bin in this mass window and multiplied by the number of bins. The combined results for the signal, combinatorial background and their ratio (S/B), showing the performance level of the HBD rejection power are shown in Fig. 34 for the mass region around the ϕ meson. The blue points are the signal, the red points are the combinatorial background and the green ones are the S/B ratio. As seen in Fig. 34 approximately 40% of the signal survives all steps whereas the S/B ratio improves by a factor larger than 100.

6.7 Signal to Background Ratio

The HIJING generator gives only the combinatorial background which originates from γ conversions and π^0 Dalitz decays. However at RHIC energies, electrons from the decay of charmed mesons become a significant source. This is illustrated in Fig. 35 which presents an absolute comparison of the various sources of electrons (from hadron decays and charmed decays) as well as their associated combinatorial backgrounds. Since the calculations for the charm decays were done for central Au+Au collisions with a charged

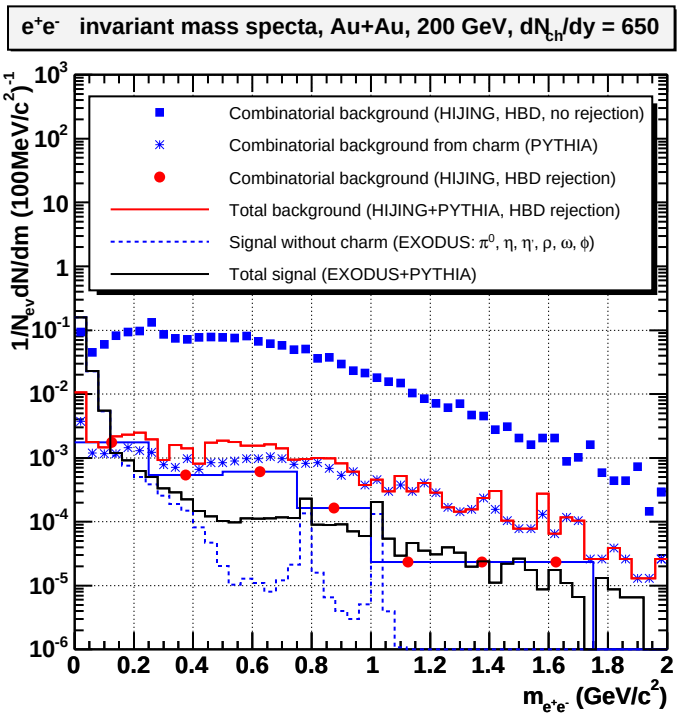

Figure 35: Absolute comparison of signals and backgrounds with and without HBD and with electrons from charmed decays.

particle multiplicity of $dN_{ch}/dy = 650$ per unit of rapidity and with ideal electron identification we scaled down our HIJING results, which were obtained with $dN_{ch}/dy = 940$, by the factor $(650/940)^2$ and corrected for the pair reconstruction efficiency derived from $\phi \rightarrow e^+e^-$ events merged with HIJING events. The background extracted from HIJING events without HBD is shown in Fig. 35 as the blue squares whereas the reduced combinatorics using the HBD rejection power is shown by the red dots. The combinatorial

background from charm decays calculated using the PYTHIA generator is shown by the blue stars. It is seen that the latter, which is negligible in the present set-up of PHENIX, becomes the dominant source of background once the HBD rejection power is turned on. The red histogram represents the total background (from γ conversions, π^0 Dalitz decays and charm) after HBD rejection, whereas the black histogram represents the total expected signal from the known hadronic sources calculated using the EXODUS generator (dashed blue histogram) and from charm calculated with Pythia. As seen in Fig. 35 with the HBD, the overall improvement in the S/B ratio is remarkable. For instance, at $m_{e^+e^-} = 0.4$ GeV/c^2 the signal to background ratio improves from 1/520 to 1/5, at $m_{e^+e^-} = 0.78$ GeV/c^2 (ρ/ω peak) it increases from 1/200 to 1/4, at $m_{e^+e^-} = 1.02$ GeV/c^2 (ϕ peak) from 1/100 to 1/2.

7 Readout Electronics

7.1 Hybrid Preamps

Since the total number of readout channels for the HBD is relatively small (2304), and the size of the readout pad is rather large ($\sim$7 cm^2, thus providing ample space per channel on the readout board,) it is possible to use discrete hybrid preamplifiers for the charge input signals from the GEMs, as opposed to having to develop a new ASIC preamp for this application. We have chosen to use a new hybrid preamp, the IO1195-1, developed by the Instrumentation Division at BNL. This preamp is a variation of several earlier devices developed for similar applications which has been adapted for use with the HBD. The schematic diagram is shown in Fig 36. It is designed for bipolar input (to be used with negative inputs for the HBD), and drives a differential output to a 100 ohm cable which delivers the signal to a shaper located in the Front End Module (see next section). The gain is set to give an output signal of $\pm$ 100 mV for an input signal of 16 fC (100,000 e's), which corresponds to an average signal of 20 photoelectrons per pad at a gas gain of 5×10^3. The preamp output has a maximum dynamic range of $\pm$ 1.5 V, corresponding to an input signal of up to 300 p.e. The noise was measured with the prototype preamp connected to a GEM detector with a geometry similar to the HBD and found to be $\sim$1100 e's, which would give a signal-to-noise ratio of $\sim$100:1 for the average input signal. The preamp operates with $\pm$ 5V and draws 165 mW per channel. The design of these preamps is now complete and the total number needed for the entire HBD can be ordered and delivered within a few months.

The preamps will be mounted on a readout board which forms the backplane of each detector panel. The inner surface of the detector panel consists of the hexagonal pad plane and is connected through a honeycomb layer to the back readout plane, as shown in Fig. 25. The wires are soldered at each end and the two outer boards are glued to the honeycomb, thus forming a gas seal. The readout board is a multilayer board which contains the preamps and has a signal layer which drives the differential output signals from the preamps to connectors located at the edge of board. The signals are then transported by individually shielded cables to the input of the Front End Module, as described in the next section. The readout board also has provision for distributing a test

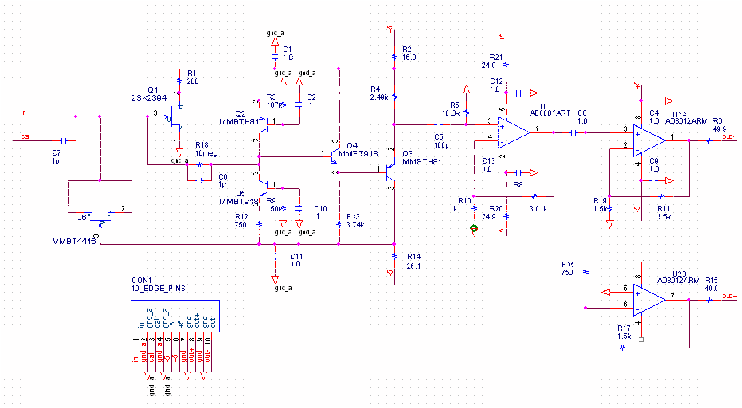

Figure 36: The IO1195-1 hybrid preamp.

pulse to the input of each preamps.

7.2 Front End Module

The HBD Front End Module (FEM) has the function of receiving the HBD preamp signals, digitizing them, and sending them to Data Collection Module (DCM) and HBD Local Level 1 modules (LL1). The FEM will be hosted in 6 VME crates located near the detectors. Each FEM will receive signals for 48 channels. A custom dataway will be used as a bus for the serial data and will chain FEM data between adjacent modules. A crate interface module will be used to interface with the PHENIX Granule Timing Module (GTM) as well as for the PHENIX slow-download interface. The Level 0 (L0) and Level 1 (L1) timing signals and serial data will be generated from the interface module and sent to the FEM.

7.2.1 FEM

The amplified differential signals will be driven from the detector to the FEM through 2mm Hard Metric (HM) cables. The cable consists of 2 isolated 26 gauge parallel wires with an overall shield and has an impedence of 100 ohms. The 2mm HM connector has 5 pins per row, and can host 2 signal pairs plus a central ground pin per row.

The overall block diagram for the FEM is shown in Fig. 37. The cable receiver, as shown in Fig. 38, receives and shapes the signal and drives a differential output to the ADC. Currently the receiver is configured with 60% gain. However, the final gain adjustment can be done by changing the feedback resistors. Fig. 39, shows the PSPICE simulation for a 16 fC signal after the receiver.

An 8 channel 65 MHz 12-bit ADC will be used to digitize the signal. The ADC will sample the signal 6 times per RHIC beam crossing at $\sim 6\times$ 9.4MHz. Ignoring the voltage shift of the ADC, the full range of the ADC is +1V to -1V. However, the amplifier and receiver arrangement can only swing the voltage from 0V into the positive direction.

The 12 bit ADC will produce 11 bits of useful information. With the proposed gain setting, a 16 fC signal will produce ∼150 ADC counts. The ADC data is serialized at 12 times the sampling clock frequency of ∼720 MHz. An FPGA will be used to receive the

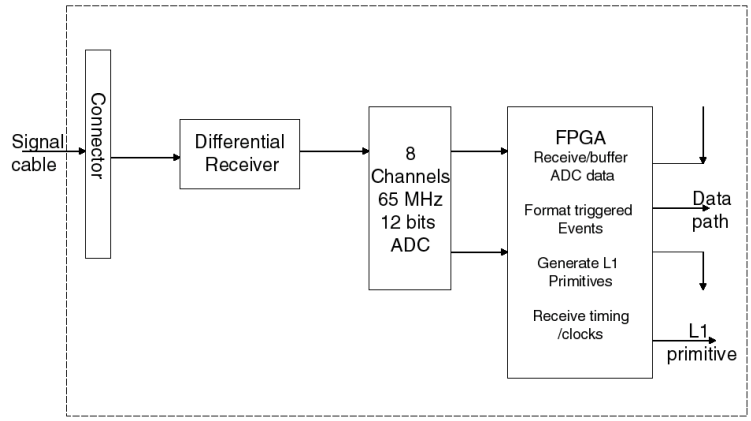

Figure 37: Overall layout of HBD Front End Module.

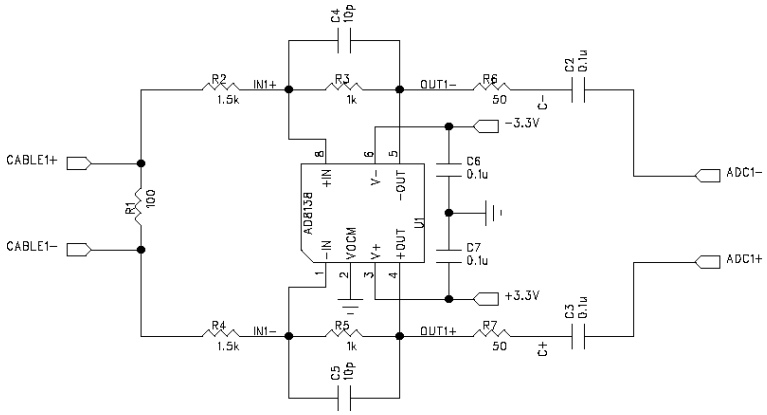

Figure 38: Cable receiver for the HBD FEM.

serial data. The same FPGA will provide the 40 beam crossing L1 delay buffers, five L1 trigger event buffers, and data formatting. Upon receiving the L1 trigger, 12 samples of data per channel will be output to the DCM at 6 times the beam crossing clock frequency. The data output of the FEMs will be connected through a token passing dataway, and every 4 FEM modules will generate an optical output to the DCM. Each channel will also output 3 bits of discriminated data to the HBD LL1 module based on the ADC data per beam clock. The trigger will allow up to 7 discriminated levels per channel which can be set by a serial download.

7.2.2 Crate Interface

The FEM crate interface receives the GTM optical signals. The clock, L1 trigger, and reset will be sent to individual FEMs via cables. The interface will be provided by a 10/100 Mbit Ethernet connection. It will also serve as a slow-download connection to the

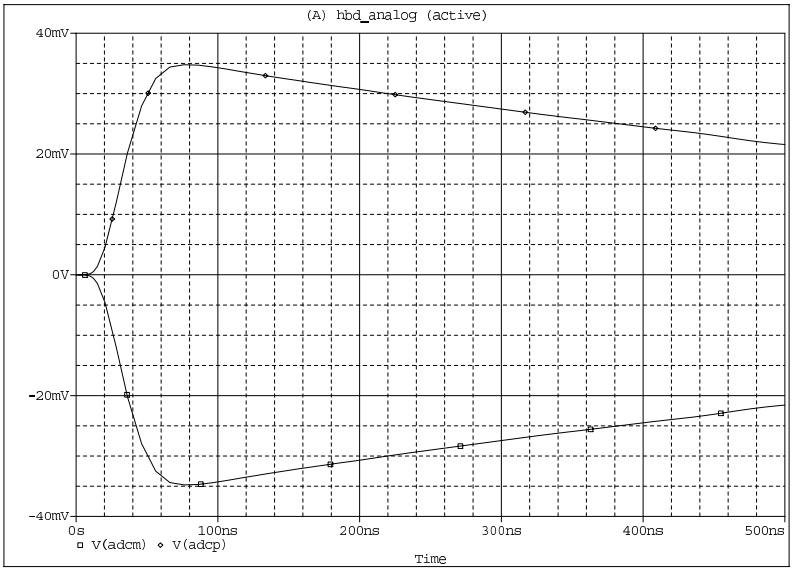

Figure 39: PSPICE simulation of a 16 fC signal at the output of the cable receiver.

PHENIX slow control system.

8 Trigger

The HBD readout is being designed so that Level-1 trigger information will be available. The HBD LL1 module receives L1 data from the FEM. Although there is currently no firm L1 trigger algorithm, L1 triggers could be received through several large FPGAs and provide the engine to form the LL1 trigger output and provide trigger summary information to the DCM upon receipt of the L1 trigger. There are ideas and plans to derive a pair electron trigger for low mass vector mesons. The HBD might also make possible a trigger for high-p_T charged hadrons - a valuable capability that PHENIX currently lacks. In the next sections, we discuss briefly the physics motivation for these triggers, and possible implementations.

8.1 Using the HBD in a Trigger for Low Mass Vector Mesons

Studying the physics of low mass vector mesons in the hot/dense medium relies on a good understanding of their behavior in pp collisions. In PHENIX, an electron trigger has been developed using the signal from the RICH and EMCal detectors. However, it cannot efficiently trigger on low-mass electron pairs with high enough rejection. For example, the current low-mass electron-pair trigger requires two RICH trigger tiles to fire, and has a rejection factor of 80 in pp collisions. The collision rate is expected to be a few MHz in the coming high luminosity pp runs. With 1 kHz bandwidth assigned to this trigger, one needs to prescale it by at least a factor of 13, which will significantly deteriorate our ability to get an accurate reference measurement from pp collisions. Therefore, an efficient low-mass electron pair trigger with much higher rejection power is needed. The HBD can be used to form such a trigger.

Table 4: Rejection factors for different distance cuts.

Threshold Distance	5 Cells	10 Cells	15 Cells	20 Cells	25 Cells
Super Cell	500	606	769	952	1053
Single Cell	278	317	385	455	500

The HBD trigger algorithm rejects backgrounds by exploiting the difference in opening angle between electron pairs originating from background and signal. The background electron pairs, e.g. Dalitz decay, have a much smaller opening angle compared to those from low mass vector mesons. The trigger algorithm then includes the following three steps:

1. If only one trigger tile fired in a event, the event is considered to contain only background and is rejected.

2. If more than one trigger tile fired in a event and no pair of hits has a distance larger than a threshold value, this event is considered to contain only background and is rejected.

3. If neither step 1 nor 2 are satisfied, the event is considered to contain a low vector meson and is accepted.

There are two ways to form trigger tiles:

- The simplest one is to treat each single pad or cell as one trigger tile (i.e. single cell method). In one blob, the cell with maximum energy deposition contains most of the energy of the blob and is well distinguished from the other cells fired by noise. One can set an energy threshold and let the trigger fire if any cell energy is above this threshold.

- The other way is to group the cells in a certain fashion and the grouped cells are considered as one trigger tile (i.e. super-cell method). In the current study, we group nine cells together to form one trigger tile. The tiles overlap to avoid inefficiency. This is illustrated in Fig. 40. The advantage of this method is that the trigger tiles fired by real tracks are better distinguishable from those fired by noise. Therefore, a higher threshold can be applied and this results in a higher rejection factors.

Table 4 shows the rejection factor as a function of trigger tile distance. As one can see, the minimum rejection factor of this new trigger is 4-6 times higher than the current low-mass pair electron trigger. The efficiency depends on the p_T of the signal and the threshold of the distance cut, and is still being studied.

8.2 Triggering on High p_T Charged Hadrons in Polarized pp Collisions

8.2.1 Physics Motivation

The discovery that very little of the spin of the proton is carried by the quarks came as a great surprise. The remainder must be carried by gluons and orbital angular momentum,

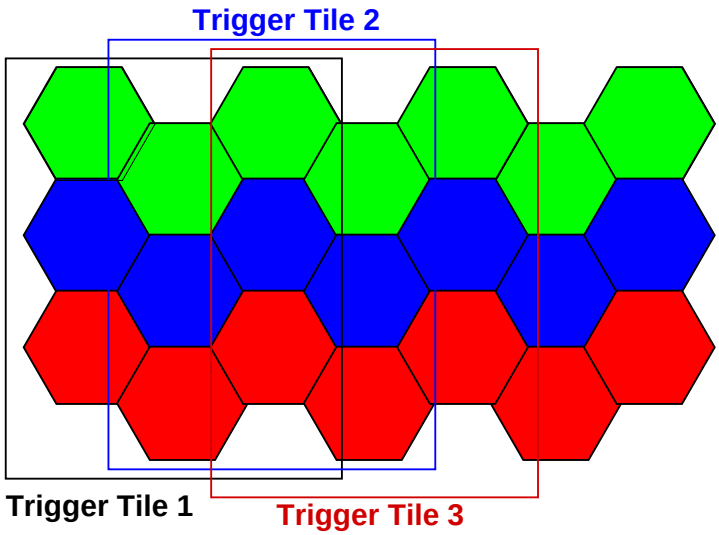

Figure 40: Nine cells combine to form a super-cell trigger tile.

but these contributions have not been measured. Collisions of polarized protons at RHIC represent a unique opportunity to measure directly the contributions of the gluons to the spin of the proton.

As a means of accessing the polarization of the gluons in the proton, one can look for differences in high-p_T single-inclusive hadron production from polarized pp collisions depending on whether the incident protons had like or unlike helicities. PHENIX has already published such an analysis on the spin-dependence in the production of π^0, $A_{LL}^{\vec{p}\vec{p}\to\pi^0 X}$. Below, we discuss briefly why we would like to be able to extend this analysis to high-p_T charged hadrons.

First we note that we are restricted to high-p_T processes for several reasons. The theoretical interpretation of the observed scattering rates involves convolutions over the polarized quark (Δq) and gluon distributions (Δg) of interest, a $2 \to 2$ partonic hard-scattering, helicity-dependent, cross-section calculable in pQCD, and in the case of hadron production, the fragmentation of one of the outgoing partons into the detected hadron. Factorizing and interpreting the process in this manner requires at least one hard scale - usually p_T. High-p_T processes are more reliably interpreted in the framework of NLO QCD since they have a reduced uncertainty on unphysical factorization and renormalization scales. Also, the perturbative corrections to the hard scattering are better understood. These arguments imply that interpreting spin-depdendent asymmetries in the production of almost any final state in polarized pp scattering is much more reliable when the process involves high momentum transfer.

Why are charged hadrons interesting? Although Δg is expected to be large and positive, our current knowledge of Δg extracted from scaling-violations in spin-dependent deep inelastic scattering does not even determine the sign of Δg. However, for $\Delta g > 0$, we expect $A_{LL}^{\vec{p}\vec{p}\to\pi^+ X} > A_{LL}^{\vec{p}\vec{p}\to\pi^0 X} > A_{LL}^{\vec{p}\vec{p}\to\pi^- X}$. With an efficient trigger for high-p_T hadrons, we could make measurements of comparable statistical sensitivity and importance to A_{LL} for π^0, and definitively determine the sign of Δg.

In addition to reasons related to the interpretation of the data, the relative importance of the various underlying scattering processes changes with p_T. In the case of π production, above a p_T of about 7 GeV/c, qg scattering dominates over gg scattering. This is important because at low p_T we are sensitive to $(\Delta g)^2$ which involves a sign ambiguity, whereas at high-p_T we are sensitive to $\Delta q \times \Delta g$. Since Δq is much better known than Δg, the interpretation of this high-p_T data should be more reliable, and there should be no sign ambiguity.

Due to the sophisticated theoretical machinery required to interpret the data in terms of polarized parton distributions, having many observables enables valuable consistency checks - such as Δg extracted from direct photons being consistent with that from π^0, π^+, and π^-. Using high-p_T final states ensures that uncertainties from higher order corrections are manageable. For these reasons alone, the polarized pp program of PHENIX would be strengthened with a new ability to trigger on high-p_T charged hadrons.

8.2.2 A Possible High-p_T Charged Hadron Trigger with the HBD

Detailed simulations have yet to be performed on the possible use of the HBD in a charged hadron trigger. Here we discuss in general terms a possible implementation of the HBD in a trigger for charged hadrons produced in pp collisions.

High momentum charged hadrons from the collision vertex and above the Čerenkov threshold in both the HBD and RICH would fire trigger elements in those detectors, and deposit some energy in the EMCal. Unfortunately, the energy deposited is often below the lowest EMCal trigger threshold. At $\sqrt{s}$=500 GeV/c, when the gain of the calorimeter is reduced (and so the corresponding lowest trigger threshold is increased) the trigger efficiency of the EMCal to hadrons will be further reduced. This suggests that for a high efficiency trigger we could try to incorporate PC3 in a triple coincidence with the HBD and RICH.

Of course, low momenta electrons would also fire the HBD, RICH, PC3, and the EMCal. Since we anticipate that the PHENIX magnets will be run in the '++' configuration during pp runs, these electron tracks would be easily distinguished by their much greater curvature (see Fig.41). To reject this background, the triple coincidence of the HBD, RICH and PC3, should incorporate a lookup table that selects the slightly curved tracks we expect from high momentum charged hadrons. We note that this trigger will also fire on muons above the Čerenkov threshold in the RICH ($\approx$ 3.7 GeV/c). Also, the substantial background from electrons from photon conversions at radii beyond the HBD which fire the RICH and EMCAL, will not fire this trigger. The proximity of the HBD to the interaction point and the fact that the highest photoelectrons/pad will occur for tracks originating from the pp collision vertex should improve its rejection power.

In pp collisions, the HBD can coexist with the silicon barrel vertex detector upgrade by being moved to a greater radius from the beampipe. The conversion of photons in the Si layers will become a new background source of electrons and positrons that will fire the HBD, RICH and PC3. Such sources will typically be softer than the hard charged hadrons of interest, so they will bend in the '++' field. This will smear out the Čerenkov photons over a stripe of pads in the HBD compared to the hadrons whose Čerenkov photons will still occupy only 3-4 pads. Restrictions on the cluster size might be a useful element in

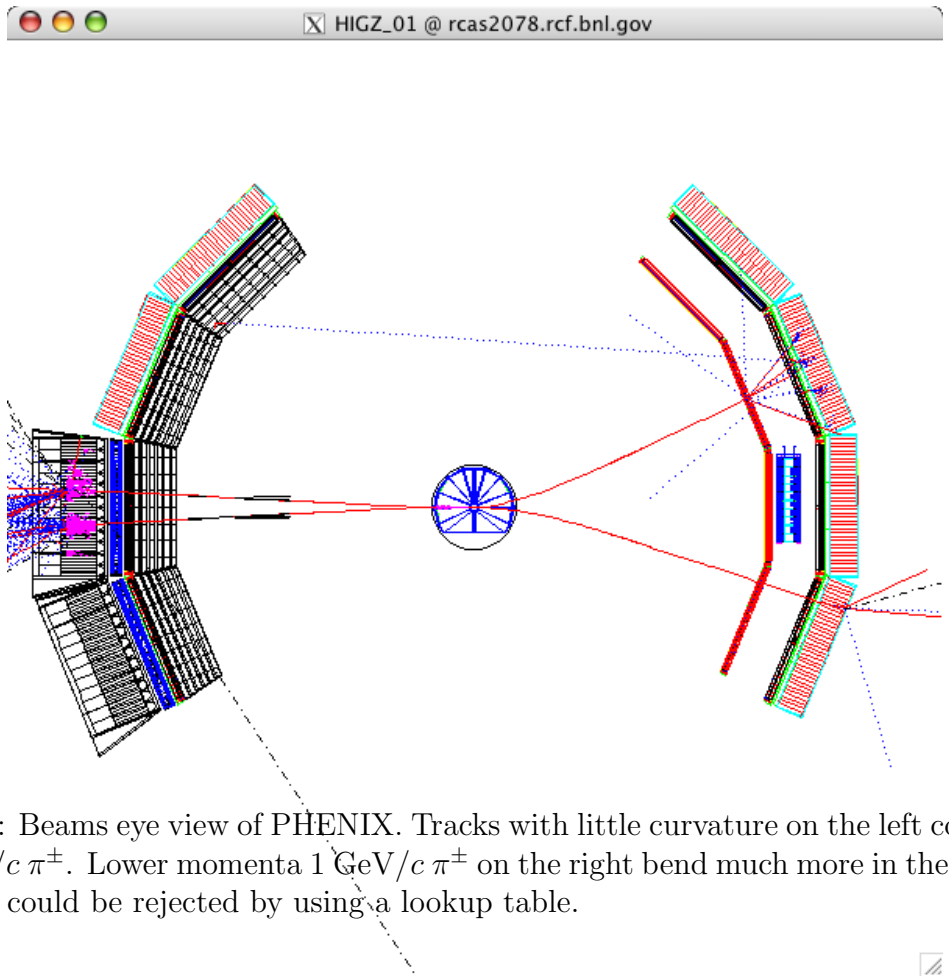

Figure 41: Beams eye view of PHENIX. Tracks with little curvature on the left correspond to 6 GeV/c $\pi^{\pm}$. Lower momenta 1 GeV/c $\pi^{\pm}$ on the right bend much more in the magnetic field, and could be rejected by using a lookup table.

any trigger incorporating the HBD.

Detailed studies are clearly required to see if the trigger outlined above can be made with high enough efficiency and rejection power to work, even in the absence of the Si detector. If a viable scheme is found, we can investigate the reduction in performance expected when the Si detector is moved into place.

9 Gas System

Maintaining high gas purity will be a critical factor for the overall performance and operation of the HBD. The detector will use a single, common gas volume for both the Čerenkov radiator and operating gas for the GEM. For the Čerenkov radiator, it will be extremely important to provide good optical transmission deep into the vacuum ultraviolet region (∼110 nm) in order to achieve the high figure of merit N_0 required to obtain the expected number photoelectrons for each electron track. Unfortunately, even small amounts of water and oxygen can produce strong absorption in the deep UV which can result in a significant loss of photons before they reach the CsI photocathode. Figs. 42 and 43 illustrate this point, which show the transmission through 36 cm of gas (in this case argon, but the same effect would be true for CF_4) as function of ppm levels of water and oxygen. Since the Čerenkov spectrum increases as $1/\lambda^2$ with decreasing wavelength, the absorption at shorter wavelengths must be kept to a minimum, thus requiring water and oxygen levels to be kept at the few ppm level or better.

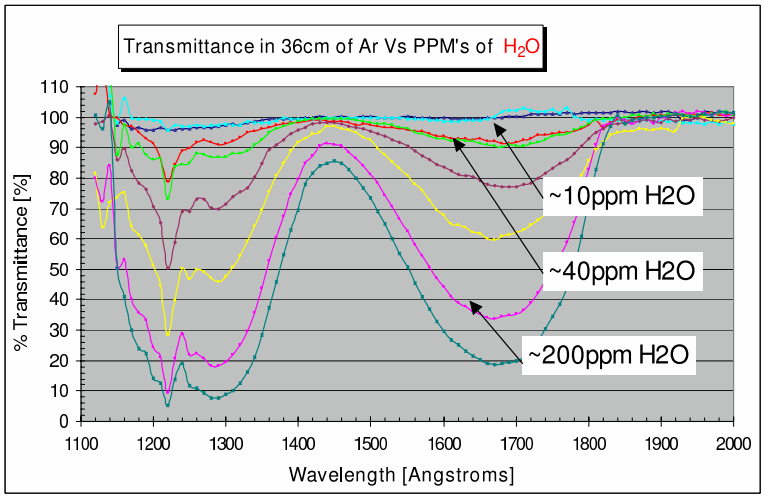

Figure 42: Transmittance through 36 cm of argon gas as a function of water level concentration.

In order to achieve the high level of gas purity required, the HBD gas system must be designed to be extremely clean and leak-tight leading directly up to the detector. In addition, the use of pure CF_4 imposes additional requirements on the types of materials and instrumentation that can be used. CF_4 is a very agressive gas which can attack numerous types of materials that are often used in detector construction (e.g., teflon, viton O-rings, etc). Fortunately, there has been considerable work done on studying the types of materials that are compatible with CF_4 as they apply to detector performance and long term aging [31]. The conclusion is that a leak-tight, CF_4-compatible gas system can be built, but special care must be paid to the types of materials and instrumentation used.

Fig. 44 shows a preliminary design of the HBD gas system. It is a quasi-recirculating system in which gas is first cleaned and purified, then pased through the detector and collected in a buffer storage tank at the output of the system. Gas accumulated in the storage tank is then compressed into cylinders which can then be taken and attached to the input of the system for re-purification and reuse. All gas lines, including the long delivery lines coming from the PHENIX Gas Mixing House, will be made of stainless steel, and all joints will be welded wherever possible. Water and oxygen monitors will be installed to closely monitor the purity level of the gas going into the detector. All mass flow controllers and gas monitoring instrumentation will use all metal seals and components wherever possible, and will have no materials known to be incompatible with CF_4.

In addition to monitoring the water and oxygen levels of the input gas to the detector, a separate gas monitoring system will be installed which will monitor the UV transmission of the gas going into and coming out of the detector. This system, shown in Fig. 45, will consist of a high-intensity Hg lamp with a scanning monochromator to measure the gas transmision over the wavelength range of 110-200 nm. This will permit constant monitoring of the actual gas transparency, which is a critical factor in determining the photoelectron yield, and detect any changes due to increased levels of oxygen, water or

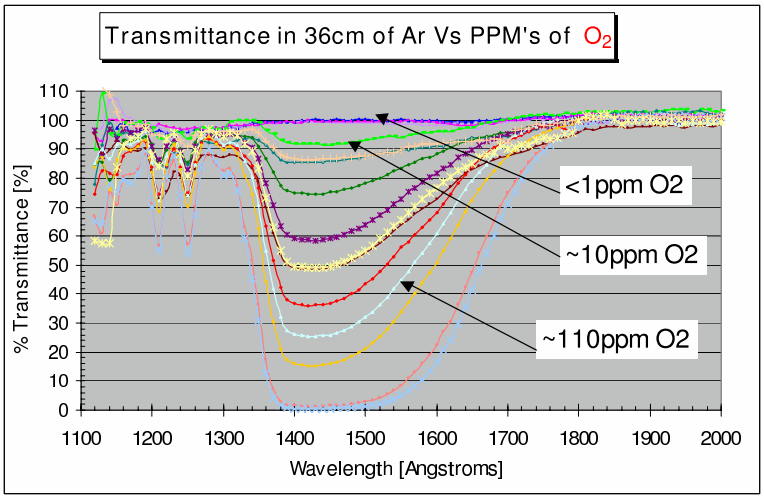

Figure 43: Transmittance through 36 cm of argon gas as a function of the level of oxygen concentration.

any other impurities which may affect the transmission. The gas monitor will measure the transmission of the common input gas, as well as the output gas of each half of the detector separately, and compare it to a reference gas cell. This will insure that any contamination due to the detector itself, as may be caused by leaks, outgassing etc., would be detected. The system will utilize a high power (150 W) Hg lamp to deliver a high flux, collimated beam of monochromatic light to each of four gas cells using a translating mirror which is moved by a remote controlled stepping motor. Due to the high beam flux, vacuum photodiodes with CsI photocathodes can be used to measure the beam passing through each gas cell which will insure good operational stability. While the entire gas monitoring system will be vacuum compatible, and will be used in this mode for initial setup and testing, it is envisioned that the system will be operated in purge mode with pure argon when it is installed in PHENIX.

10 Detector Assembly and Testing Facility

10.1 Detector Assembly

The construction of the HBD detector will be done at the Weizmann Institute of Science. The detector vessel and the GEMs glued to frames will be shipped to Stony Brook University where the CsI layer will be evaporated on the top GEMs and the detector modules will be assembled and tested. The sealed detector will be transported to BNL and installed in PHENIX. In order to successfully accomplish this task we need a CsI evaporation facility and a detector assembly area at Stony Brook University.

10.1.1 CsI Evaporator

The evaporation facility that exists at SUNYSB needs to be upgraded to improve its reliability. This facility was used to produce several successful photocathodes, however

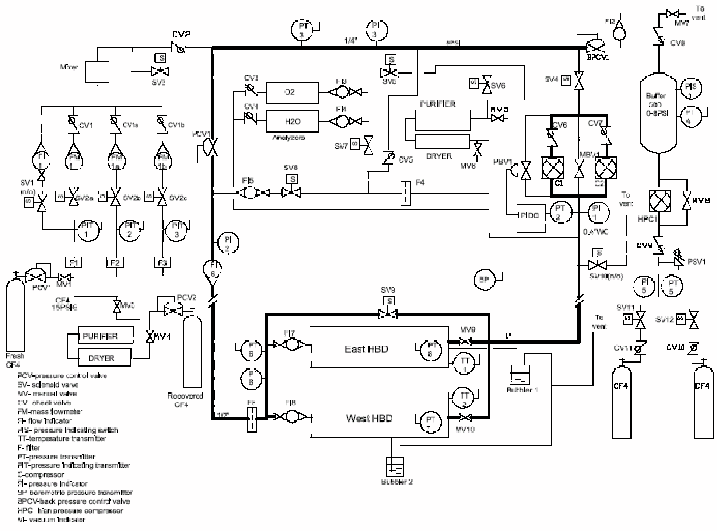

Figure 44: Preliminary design of the HBD gas system.

its reliability is poor for the production of the large number of photocathodes needed for the entire HBD project. Old elements should be replaced and the cleanliness should be increased by replacing a diffusion pump with an oil-free turbo-pump unit.

The evaporation facility is large enough to work on GEMs of the desired size. An uniformity test was done to ensure the same thickness of the CsI across the full GEM surface. The results show thickness uniformity to be $\pm 3\%$ on an area of 25 cm by 25 cm.

Exposure of the CsI photocathodes to air should be minimized, therefore the photocathodes will be placed in dessicators immediately after production and then transferred to a storage place in dry gas atmosphere. It is desirable to measure the photocathode quantum efficiency after evaporation. Current setup existing at BNL needs some modification to accommodate the final size of the photocathode.

There is a possibility to organize the mass production of the CsI photocathodes for the HBD at Jefferson Lab, where a very advanced facility to produce large-size photocathodes is operational. This facility also provides x-y scanning and monitoring of the CsI quantum efficiency and does not expose the CsI to air at any time.

10.1.2 Glove Box

The final assembly of detector modules and installation in the HBD vessel shall take place in a clean and dry environment. Such requirements can be met by using a glove box (GB) with the following parameters:

- Dimensions: 2.5m long; 1.5m tall; 1.3m wide.
- A positioning system inside the GB should be made to rotate and secure the vessel in a convenient position to work on a particular sector.
- 3 pairs of gloves on each side close to the GB bottom. Additional gloves can be used to handle the top of the detector if needed.

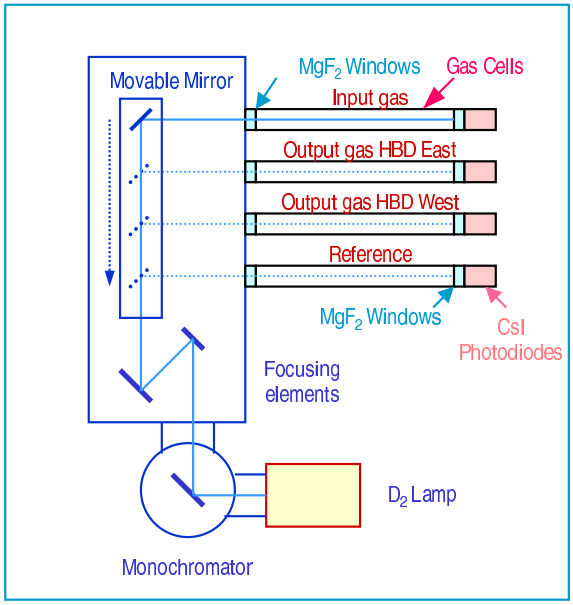

Figure 45: Gas monitoring system

- Gas flow of approximately 250 $l/hour$ (N_2). Additional water absorption elements in the gas system, forceful ventilation inside the box and humidity control devices.
- The GB should have a door to move the detector in an out on one side and an antechamber on the other side. It should be possible to pump the antechamber to several torr of air pressure with an oil free pump.
- Electrical and gas feedthroughs are needed to bring power and gases other than N_2 to make a leak test of the detector volume after final assembly. It should also have an N_2 pressure gun and pressure valve.
- The GB should have storage places for detector parts (first of all the CsI photocathodes) and other materials and clean tools.

The assembly procedure will be finalized during the work with the detector prototype in the summer 2005. The major operations of the final detector production would include the following steps:

- Production and testing of the photocathodes.
- Mounting and testing of each detector module inside the GB.
- Detector sealing and gas leak tests inside the GB.
- Electronics assembly outside the GB at SBU.
- Transportation of the detector to BNL.
- HBD integration in the PHENIX services including DAQ, arc-net, low voltage, high voltage and gas supply systems.

- Detector commissioning.

10.2 Detector Testing

The subsection above refers to operations with both the prototype and the final detector. This section describes the testing procedure of the prototype. Based on the test results with the prototype the work necessary to be done on the final detector will be established.

10.2.1 Full Scale Prototype

Testing of different detector modules is done at the construction stage and then the detector is assembled. At different steps the following quality control operations should be performed.

- The GEM foils glued on frames are to be tested for leakage current and gain uniformity. All GEMs should sustain at least 600 V in dry air and deliver a few nA leakage current.
- The detector volume will be tested for leaks before shipment to the USA and after final assembly in the GB at SUNYSB.
- The sealed detector volume will be tested for H_2O and O_2 while being flushed with N_2.
- The electronics will be tested separately to meet the design parameters.
- The photocathode after evaporation will be tested for quantum efficiency.

After the prototype is assembled it will undergo several tests.

The detector gas will be monitored for optical transparency using the monochromator at BNL. Together with the measurement of the H_2O and O_2 content it will allow to determine the parameters of the gas flow required in the final detector for optimal radiator transparency.

A low intensity ^{55}Fe radioactive source will be installed inside the detector prototype volume opposite to the instrumented part to allow the measurement the detector response to ionizing radiation. This setup will allow to map out the detector electronics, to measure the detector gain, gain uniformity, gain variation with temperature and atmospheric pressure and some long term effects previously observed during the R&D stage [32].

A small LiF window will be mounted in the panel opposite the instrumented area to allow a UV lamp from outside to illuminate the CsI photocathode. It will make possible to monitor the quantum efficiency of the prototype under realistic conditions.

10.2.2 Small Scale Prototype

A small scale prototype of the HBD detector made out of realistic materials is constructed at BNL. It has a 10×10 cm^2 detector element and a 50 cm long radiator, readout plane and electronics as foreseen for the HBD. It will be installed in the electron beam at the LEGS facility at NSLS to measure the figure of merit N_0.

The electrons comparable to full NSLS energy (2.8 GeV) deflected from the beam by Bremsstrahlung or Compton scattering against the visible laser photon beam are passing through the LEGS tagging system. The tagging system measures the electron track position in space to determine its momentum. Behind this system there is a space where the small scale prototype can be mounted inside the beam. The HV and LV systems as well as the trigger and the DAQ of the LEGS experiment can be used. This beam testis scheduled in the spring 2005.

11 Responsibilities, Cost and Schedule

In this section we outline the proposed management organization of the HBD and the responsibilities of the various groups within the project. We present the estimated total construction and installation cost, and the corresponding funding plan. Finally we present the planned schedule for construction of the HBD.

11.1 Project Management and Responsibilities

The organization and management of the HBD effort will be similar and will follow the same pattern of other upgrade projects of the PHENIX experiment.

The construction, testing and assembly activities, as well as the detector commissioning and operation, trigger and software development, will be carried out in a joint effort of a consortium of the following PHENIX groups:

- Brookhaven National Laboratory,
- Columbia University
- Florida Institute of Technology
- RIKEN-BNL Research Center
- Stony Brook University
- Center for Nuclear Studies, Tokyo
- Weizmann Institute

In particular, most of the construction, testing and assembly work will be mainly carried out by students of CNS, FIT, SBU and Weizmann.

The responsibility for the HBD subsystem will be shared by the subsystem leader, Itzhak Tserruya (Weizmann Institute) and his deputy, Alexander Milov (SBU and BNL). The subsystem leader shall report to PHENIX management and represents the HBD consortium in the DC. Clear roles and responsibilities for the various construction tasks have recently been defined:

- Detector vessel construction and pretest of GEM foils: I. Ravinovich (Weizmann)
- CsI evaporation, assembly and testing of triple GEM detector elements: A. Milov (BNL,SBU).
- Monitoring systems: C. Woody (BNL)
- Gas system: B. Azmoun (BNL)
- Trigger: D. Kawall (RIKEN-BNL)

- Analog Electronics: C. Woody (BNL)
- Digital electronics C. Chi (Columbia)
- On-line monitoring: S. Oda (CNS)

The same people who build the detector will commission it and provide expertise to the PHENIX collaboration to operate the HBD and provide physics data for the collaboration to use.

Once installed and commissioned, the HBD will become a subsystem similar to other, already operational, parts of PHENIX. Operation of the HBD will then be part of operating the PHENIX experiment, and routine work and performance monitoring will be performed by the scientists on PHENIX data taking shifts. The consortium building the HBD will provide the leadership, expertise, and scientific manpower for the more complex aspects of HBD operation and maintenance.

11.2 Total Cost Estimate and Budget Justification

Table 5 gives a detailed cost-breakdown of all components of the HBD, including the detector itself, the assembly and testing facility, electronics, trigger, gas and monitoring systems and the infrastructure and installation costs.

The HBD construction is divided into two phases which will be carried out at two places. The first phase, the construction of the detector vessel, frame mounting and pretest of the GEM foils, will be done at the Weizmann Institute. The cost is firm, based on the experience gained over the last two years of HBD R&D and the design and construction of the full scale HBD prototype which is very close to the final design. Consequently, only an average 15% contingency is applied to this item. A total of 24 triple GEM detector modules are needed for full coverage of the HBD. The cost estimate is based on 32 such modules, i.e. 33% spares.

The second phase will be carried out at SBU and includes evaporation of a thin layer of CsI on the top GEM foil of each detector module, measuring its quantum efficiency, testing each module and assembling it into the detector vessel. An assembly and testing facility will be set-up at SBU. A clean room is needed for handling the GEM foils. CsI is very hygroscopic and thus all the subsequent handling after evaporation (stacking in triplets, test with ^{55}Fe X-rays and UV lamp, and assembly in the HBD vessel) must be done inside a high-quality glove box. A large clean tent and an existing evaporator at SBU will be used. The cost includes refurbishing the clean tent as well as the costs for a new turbo pump to improve the cleanliness of the evaporator setup. The costs are based on specific quotes from appropriate vendors. The CsI photocathode quantum efficiency needs to be measured after CsI deposition. This will be done using the system already existing at BNL.

The front end electronics cost included in this proposal is for purchase of 96 channels of hybrid preamplifier for each of the 24 HBD modules. The front-end electronics was designed by the BNL Instrumentation Division, and can be produced at a cost of $14.00 per channel, plus parts which are already owned by BNL. We assume a yield of 90% for this well established manufacturing technique and we plan for $\sim$ 15% spare channels. A pre-production version of the preamplifiers is in the process of being tested with triple

Table 5: Detailed cost estimate of the HBD.

	Qtty	Unit Cost	Cost	Total Cost
HBD detector				
Vessel (design, parts, workshop, tooling)	2	30000	60000	
Triple GEM detector element (with 30 %spares)	32	4600	147200	
Connectors, resistors, capacitors, supplies			22500	
Shipping			10000	
Total (including 15% average contingency)			**275655**	**$275,655**
Detector assembly and test facility				
Glove box	1		47000	
Clean room refurbishing			11000	
CsI evaporator			35000	
Total			**93000**	**$368,655**
Electronics				
Preamp. (with 10% spare)	3000	14	42000	
Front end modules (with 5 spare modules)	53	3840	203520	
Clock, Backplane and Misc.			20000	
Total (including 20% average contingency)			**318624**	**$687,279**
Trigger				
Trigger EDIA			80000	
Trigger cost			60000	
Total (including 30% contingency)			**182000**	**$869,279**
HBD monitoring systems				
Gas monitoring	1		65000	
Gain monitoring	1		10000	
Total			**75000**	**$944,279**
Gas system				
Gas system			60000	
Gas piping			20000	
Total (including 30% contingency)			**104000**	**$1,048,279**
Installation and infrastructure				
Installation			50000	
HV and LV systems			50000	
Cabling			20000	
Total (including 30% contingency)			**156000**	**$1,204,279**

GEM detector elements. No contingency is applied to this item. The HBD readout electronics is developed by Columbia University (C.Chi). Design is well underway and first prototypes should be available in May 2005. For the final production we need a

total of 48 modules, each one serving 48 channels. We are planning on 5 spare mudules. We are assuming a cost of $80 per channel based on the rich experience of the Columbia group in designing and constructing similar electronics for PHENIX. Since the choice of components is not yet finalized we apply an average 20% contingency to this item. The trigger algorithm is not yet fully specified, and consequently there is no detailed concept for the trigger implementation. A 30% contingency is applied.

During operation the gas transparency and HBD gain must be continuously monitored. The gas transparency is monitored using a monochromator system, described above. The cost estimate is based on two separate vendor quotes from McPherson; one for the major optical components ($35K) and one for a fully custom built system ($109K). We do not base our cost estimate on the later quote since we feel that the custom built system is overdesigned for our needs. Using engineering experience from past gas detector projects we are confident that we can build an adequate system for much reduced costs of $65K including all components. The HBD gas gain is continuously monitored using a standalone pilot chamber (Canary Chamber) sharing the same gas supply lines as the HBD. The HBD Canary Chamber follows the design of one we have recently built for the PHENIX drift chamber system. Consequently, the costs are well known.

The gas system is a critical element for the successful operation of the HBD. Stainless steel piping and high quality components are a prerequisite. Although detailed design and quotes are already at hand we have not yet finalized our choices. The start of the gas system construction is foreseen after completion of Run 5. A 30% contingency is applied to this item.

With the exception of the HV system which is well defined, we are just beginning to address all other infrastructure and installation issues. The cost estimate is based on general considerations (a weight of less than 10 kg per arm, a total of 2304 signal channels). This item carries a 30% contingency.

11.3 Schedule

A full scale prototype (as described in section 5), very similar to the final HBD design, is under construction at Weizmann. This prototype will be equipped with one detector module providing an excellent possibility to test all the important functional properties of the final HBD. Once the vessel construction is finished and after doing preliminary tests of tightness of the vessel, leak rates and gas purity, the prototype will be shipped to BNL for detailed tests of the whole electronic chain, preamplifiers, motherboard and FEM. A first FEM prototype is expected to be ready by the end of May 2005. It will first be tested on the bench and then with the HBD full-scale prototype.

The planned schedule for the construction of the final HBD is as follows:

- Construction of HBD vessels at Weizmann: begins September 1st, 2005, complete in 3 months; ship to SBU beginning December 2005.

- Production of GEM panels at Weizmann. The precise schedule will be dictated by the delivery of GEM foils from CERN. The foil production at CERN is scheduled to start in September 1st, 2005 (after tests on a pilot production in the summer of 2005) with an expected delivery rate of 30 40 GEMs per month. In the present

schedule we are assuming a total delivery time of 3 months. The framing and pre-testing of GEM foils will start as soon as the first GEMs arrive at Weizmann and will roughly follow the rate of GEM delivery. Shipping of mounted and pre-tested GEMs to SBU will start in October 1st, 2005 and should be completed in 3 months.

- Setting-up of the assembly and testing facility at Stony Brook should be completed before October 1st 2005, when the first framed GEMs are shipped to SBU.
- CsI evaporation at Stony Brook begins October 2005. Measurement of quantum efficiency and assembly into detector modules proceeds in parallel with evaporation in assembly-line fashion. All modules complete in January 2005.
- Final detector assembly and testing: December 2005 - January 2006. Full detector ready for installation by end of January 2006.
- Preamplifier production: begin July 2005, complete in 1-2 months.
- FEM production: begin August 2005, complete end of January 2006.
- Gas system construction at BNL: begin after completion of Run 5, complete in 2 months.
- Monitoring systems: 4 months delivery time; complete in September 2005.

This is a busy but doable schedule that will allow us to have the HBD ready for Run 6 if this run is delayed by a few months. The schedule could be relaxed if Run 6 is delayed more than that or if it is combined with Run 7. On the other hand, if it turns out that Run 6 will start as the previous runs, in the fall of 2005, we believe that we can push the schedule to have at least one arm of the HBD ready for installation in Run 6.

Appendix

A Conceptual Monte Carlo Simulation and System Specifications

Monte Carlo simulations are a necessary prerequisite for the design of any new detector. This is particularly true for the present design of a detector capable of measuring an extremely weak signal of low-energy electron-positron pairs in the face of an overwhelming background of electrons and positrons from π^0 Dalitz decays and γ-conversions and of hadrons, primarily pions.

A.1 Input Parameters

For simplicity we simulate a central Au-Au collision at $\sqrt{s_{NN}} = 200$ GeV by 3000 pions of each charge state in full space which is equivalent to

$$(\frac{dN}{dy})_{y=0} = 475$$

for each pion charge state. The p_T and y distributions are those predicted by the Hijing model.

The charged pions are tracked through the magnetic field of the PHENIX detector using look-up tables. Multiple scattering and all other physical proccesses are approximated by smearing the momentum by the amount

$$\frac{\sigma_p}{p} = 0.005 + \sqrt{1 + p^2} \tag{2}$$

We restict our calculations to particles with momentum $p_T > 200$ MeV. In the following we define *Track* a charged particle of momentum $p_T > 200$ Mev going through pad chambers PC1 and PC3. With these restrictions the total number of tracks in the two arms of the central detector is 208 per event (See also Table. 6)

The dilepton signal is simulated in our calculations by the decay products of the ϕ-meson:

$$\phi \rightarrow e^+e-$$

The ϕ-mesons were generated by a dedicated event generator and the acceptance of the initial ϕ and its decay products in the two arms of the central detector are shown in Fig. 46 which gives the rapidity and momentum distributions of the ϕ meson (left panels) and the momentum and opening angle distributions of the decay electrons in the central detector arms (right panels). Fig. 46 shows that the probability to detect a ϕ-meson in a single arm is negligible.

The total (i.e. 4π) ϕ-meson production probability is defined with respect to the total π^0 yield [33]

$$N_\phi/N_{\pi^0} = 0.015 \tag{3}$$

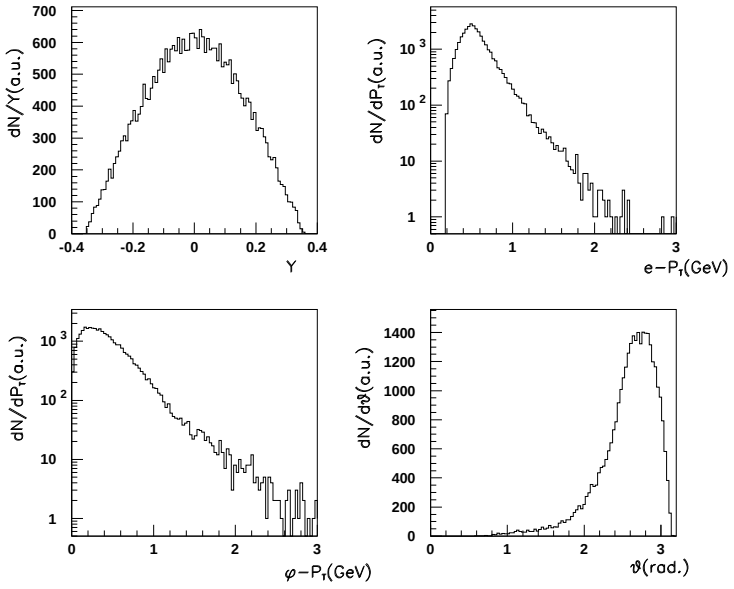

Figure 46: Rapidity and momentum distribution of the ϕ meson (left panels) and momentum and opening angle distributions of the decay electrons in the central arm detectors (right panels)

The ϕ-meson rapidity density at mid-rapidity is given by

$$\frac{(dN_\phi/dy)_{|y|<0.5}}{N_\phi} = 16\% \tag{4}$$

The acceptance of the ϕ-meson decay products $\phi \rightarrow e^+e^-$ in the two central arms with the p_T-cut of 200 MeV is

$$\frac{N_{\phi\rightarrow e^+e^-}}{(dN/dy)_{|y|<0.5}} = 2.9\% * BR \tag{5}$$

where BR = 3 * 10^{-4} is the branching ratio of the $\phi \rightarrow e^+e^-$ decay. The total number of e^+e^- pairs from $\phi \rightarrow e^+e-$ decay within the PHENIX acceptance and $p_T > 200$ MeV is thus

$$\begin{aligned} N_{\phi\rightarrow e^+e^-} &= 0.015 * 0.16 * 0.029 * 3 * 10^{-4} * N_{\pi^0} \\ &= 6.2 * 10^{-5}\phi/event. \end{aligned} \tag{6}$$

The electron background sources consist in our case of π^0 -Dalitz decays and conversion electrons. We assume a total radiation length of X/X_0 = 1 % and for simplicity we assume that all conversions are generated at the vertex. Both sources are simulated with the PISA simulation program for the PHENIX detector which yields 1.26 electron tracks

per event. The performance of the present PHENIX detector is discussed in detail in a recent Technical Note [12]. It is shown there that even under ideal conditions the *S/B* is of the order of $S/B = \simeq 1/10$. Moreover it is shown that the most critical factor for an improved *S/B* ratio is the π-rejection factor whereas one can tolerate a relatively low single-electron track efficiency.

Throughout this section we assume that the zero field region extends to $R = 60$ cm and that the magnetic field stays unchanged from its present strength above this radius. The goal is to achieve, under ideal conditions a *S/B* ratio of ∼10/1, i.e. two orders of magnitude better than the present configuration.

A.2 Particles and Tracks in the Upgraded Configuration

The number of *particles* in the inner detector and *tracks* in the outer detectors (PC1 and PC3) originating from electrons and charged pions is summarized in Table 6.

The inner detector is sensitive to all particles emitted in the fiducial acceptance, without any p_T cut. There are 9.2 electrons plus 280 charged pions per event, of which 173 can be tracked through the central arms (i.e. they have $p_T > 200$ MeV and go through PC1 and PC3). We have not included additional hits. e.g. background hits originating from the magnet poles.

In the outer detectors (PC1 and PC3) the number of electron tracks per event is practically unchanged (∼1.1 single e-tracks per event before the mass cut and ∼0.9 single e-tracks after the mass cut). The mere requirement that the outer electron track be matched to a particle in the inner detector brings already a reduction of the single electron track rate to 0.7 tracks/evt. The number of pions in the outer detectors is unchanged, 208 π /evt., of which, as stated above , 173 have a matched hit in the inner detector and the remaining 35 probably originate from side feeding. .

The rate of the ϕ meson signal has slightly increased from $6.2 * 10^{-5}$ (see eq. 6) to $7.1 * 10^{-5}$ due to the increased pair acceptance in the reduced field configuration. For the rest of this document we normalize this rate to 1 (i.e. the quoted signal rates are to be multiplied by $7.1 * 10^{-5}$ to get the true signal rate). The mass cut reduces the signal strength to 0.92 and the requirement of matched hits in the inner detector for both tracks further reduces it to 0.76 ϕ/event.

Table 6 also shows the *S/B* ratio. With the mass cut of 130 MeV/c^2, we obtain the same *S/B* ratio of 1/7 as obtained in the previous section. Requiring all electron tracks to be matched to a particle in the inner detector results in a small improvement to *S/B* = 1/5 showing a stronger reduction of the background compared to the signal.

In the following we study in detail the benefits of the inner detector in improving the *S/B* ratio. We consider four different schemes:

- inner detector with perfect spatial resolution, close-hit cut, and no particle ID.
- inner detector with perfect spatial resolution, close-hit cut and perfect electron identification
- same as 2 plus veto area
- same as 3 with finite double hit resolution

Table 6: Hits and tracks per event statistics in the Upgraded PHENIX Configuration

Particles in inner detector (no p_T cut)

electrons:	$\pi^0 \rightarrow e^+e^-\gamma$	4.1
	$\gamma \rightarrow e^+e^-$	5.1
	Total	9.2 e-hits/evt
$\pi^{\pm}$ particles:	280 π/evt = 173 tracks + 107 hits	

Tracks in outer detectors ($p_T > 200$ MeV)

e-tracks:	All:
	0.20 pairs = 0.1 π^o Dalitz + 0.1 γ conversions.
	1.10 singles = 0.5 π^o Dalitz + 0.6 γ conversions.
	Mass cut (m > 0.13 GeV).
	0.93 singles = 0.42 π^o Dalitz + 0.51 γ conversions.
	With a matched hit in inner detector.
	0.70 singles = 0.32 π^o Dalitz + 0.38 γ conversions.
$\pi^{\pm}$ tracks:	208 π/evt

ϕ Meson Signal

Rate: 7.1*10^{-5} per event	1.0
Mass cut (m > 0.13 GeV).	0.92
With matched hits in inner detector.	0.76

S/B Ratio

Mass cut (m > 0.13 GeV).	S/B = 1/7
With matched hits in inner detector.	S/B = 1/5

A.3 Inner Detector with Perfect Spatial Resolution, Close-hit Cut, and no Electron-Identification

This is the simplest option. The inner detector has no electron identification and the close-hit cut is performed for all hits in the detector (280π + $9e$). The cut is very effective in reducing the background but at the same time it also kills the signal by random close hits in the inner detector. If we set as a guideline preserving ∼50% of the signal, the close hit cut is limited to ∼25mrad, resulting in an improvement of the S/B ratio to ∼1.

We can somewhat improve the situation by limiting the close-hit cut to single hits (as

opposed to tracks) i.e. to the $107\pi + 9e$ which are not matched to the outer detectors. The close-hit cut can now be extended to ∼50 mrad resulting in a S/B ∼2. But we conclude that without electron identification we cannot achieve the required goal of S/B ∼10. The signal gets lost by random close hits in the inner detector.

A.4 Inner Detector with Perfect Spatial Resolution and Perfect Electron Identification

We assume next that the inner detector has perfect electron identification capability, so that the close-hit cut is only performed for the 9 electron hits. The results are shown in Fig. 47. The left panel shows the absolute yield of ϕ mesons per event and of background tracks per event (the contributions from γ conversions and π^0 Dalitz decays are shown separately) as a function of the opening angle cut θ_{cut}. The right panel shows the S/B ratio as a function of θ_{cut}. With the opening angle cut of ∼180mrad, a S/B ratio ∼12 is obtained while preserving ∼50% of the signal. Note that this dramatic improvement is achieved by the electron identification capability whereas the π rejection factor does not play a crucial role. As seen from Table 6 a rejection factor of ∼100 will add ∼3 fake electrons to the genuine 9 electron hits in the inner detector. The requirements of the inner detector are thus very different from those of the tracking detectors: It requires a very high electron identification efficiency but can tolerate a moderate π rejection, quite opposite to the requirements of the tracking system.

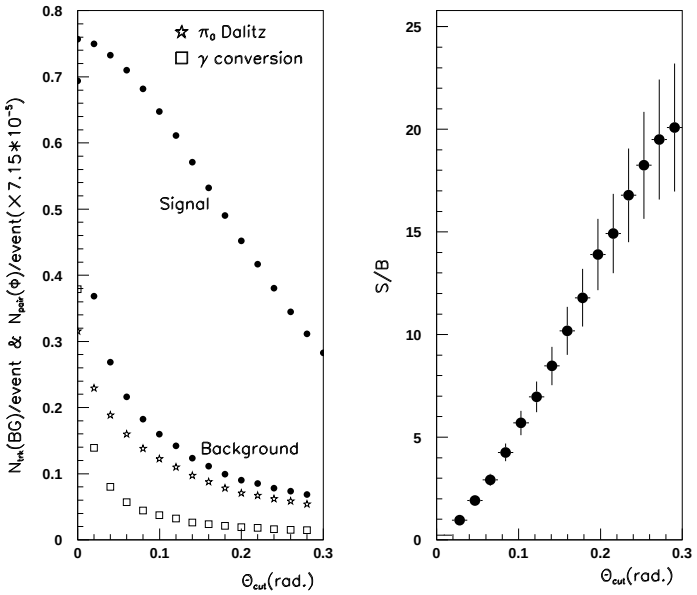

Figure 47: Left panel: absolute yield of signal pair and background tracks per event surviving the close-hit cut as a function of the opening angle cut size, assuming perfect electron identification in the inner detector. Right panel: same for S/B ratio.

A.5 Benefits of Veto Area

For large opening angle cuts $\theta > 200$mrad , the remaining background is mainly due to tracks from π^0 Dalitz decays. The conversions are reduced to a few percent. However both survive even larger cuts. This is due to the fact that the partner of these tracks is outside the fiducial acceptance of the central arms. Therefore the background rejection can be improved by adding a veto area to the inner detector i.e by increasing its acceptance beyond that of the central arms. In this subsection we study the additional benefit in the S/B ratio which we may expect from such a veto area. We increase the acceptance in both the azimuthal direction, from $\delta\phi \leq 90\,\mathrm{deg}$ to $\delta\phi \leq 120\,\mathrm{deg}$ in steps of 10 deg, and in pseudorapidity from $\mid \delta\eta \mid \leq 0.35$ to $\mid \delta\eta \mid \leq 0.50$ in steps of 0.05. The results are shown in Fig. 48. The figure shows the absolute yield of the signal and background and the S/B ratio for various acceptances of the inner detector. As before , for this calculation the inner detector is assumed to have perfect spatial resolution and perfect electron identification.

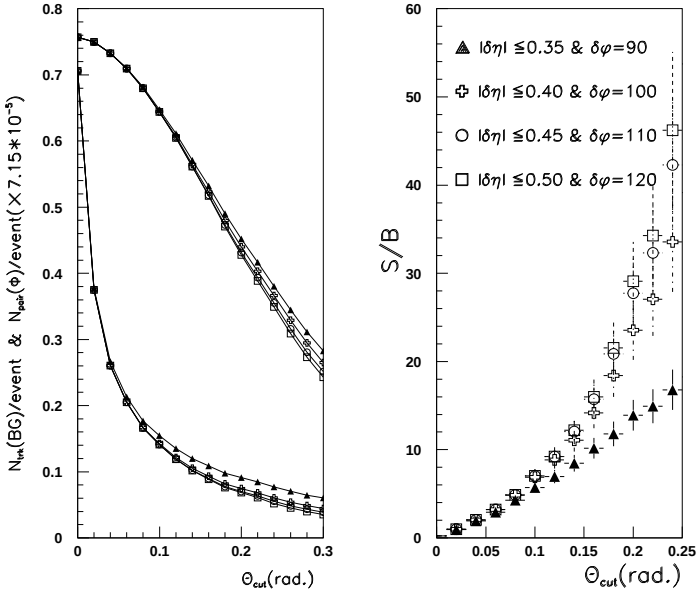

Figure 48: Left panel: absolute yield of signal pair and background tracks per event surviving the close-hit cut as function of the opening angle cut value, assuming perfect e-ID in the inner detector. Right panel: same for the S/B ratio. The different symbols refer to different acceptances of the inner detector (see right panel)

From the figure we see that most of the improvement in the S/B ratio occurs already with a modest increase in acceptance to $\mid \delta\eta \mid \leq 0.40$ and $\delta\phi \leq 100\,\mathrm{deg}$. With an opening angle cut of $\sim$180mrad, it allows us to reach a S/B ratio of $\sim$20. A further increase in the veto area brings only a small further improvement.

A.6 Double Hit Resolution

From the results of the previous section it would seem that we have reached our goal. However our study so far relied on the assumption of an ideal detector performance.

The most critical assumption is the perfect spatial resolution of the inner detector, or in other words, perfect double hit recognition (*DHR*). The importance of the *DHR* is clearly illustrated in Fig. 49 where it is seen that a sizable fraction of the rejection occurs at very small opening angles.

In this section we show how much the *S/B* ratio is affected by assuming various levels of *DHR* in the inner detector. Our assumptions are:

> If the distance between the two hits in the inner detector is larger than the *DHR*, they are assumed to be recognized as two hits. Otherwise they are merged into one hit. However, in this case the detector will show a double analog response. Hence we assume that merged hits can be recognized as a double hit with 50% probability.
>
> The rest of the assumptions remain unchanged, namely we consider an inner detector with veto area ($|\ \delta\eta\ | \leq 0.40$ and $\delta\phi \leq 100\,\mathrm{deg}$), π-rejection $= \infty$ and electron detection effficiency = 100%. We remove tracks forming a pair with $m \leq 130$ MeV in the outer detectors, and remove tracks with no matched hits in the inner detector and we apply close-hit cuts considering only electron hits in the inner detector.

We considered the following cases: *DHR* = 0 mrad (i.e the ideal case assumed so far), 10.0 mrad, 20.0mrad and 30.0 mrad. The results of the calculation are shown in Fig. 49 and Fig. 50.

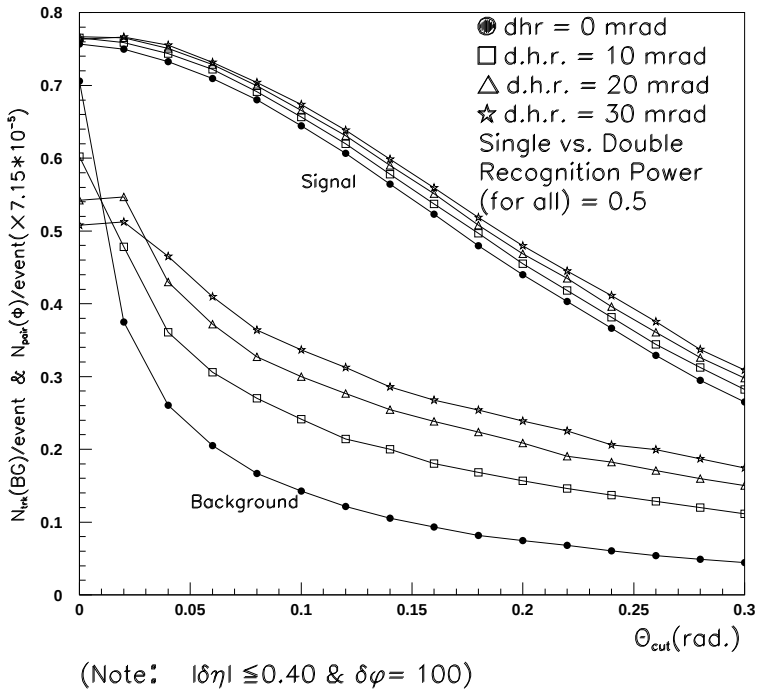

Figure 49: Signal and background for different *DHR*

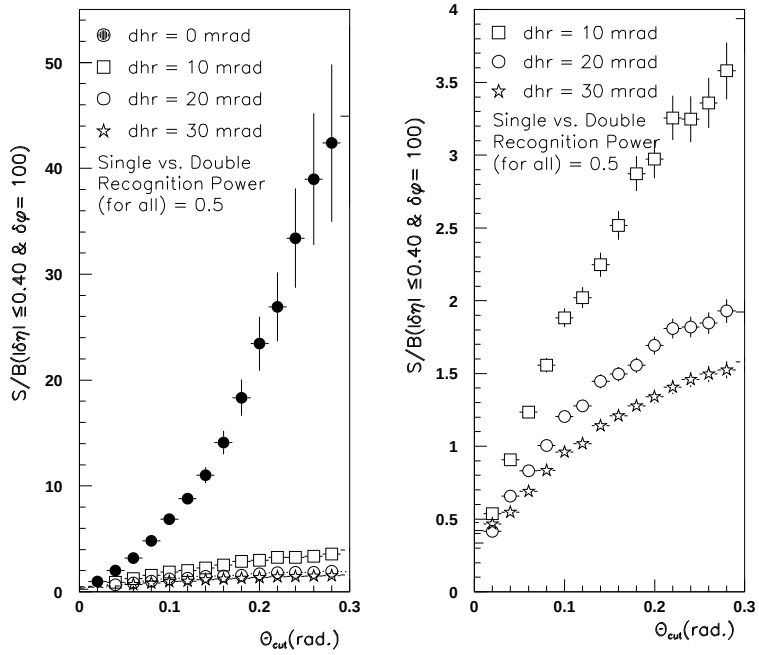

Figure 50: S/B for different DHR.

We see from Fig. 50 that the price for a finite DHR is enormous: With a DHR of 20-30mrad the S/B ratio is down to 1-1.5, more than an order of magnitude from the ideal case ($DHR = 0$). This is not a surprising result. As already stated, we need to reject γ -conversions and π^0 Dalitz decays to at least a 90% level and consequently the probability to recognize merged hits must also be at least at the 90% level.

A.7 Summary of the Monte Carlo Studies

Table 7 summarizes the the S/B results of the present study.

In order to fulfill its main goal of rejecting the background electron tracks, the inner detector must have an excellent electron identification capability ($> 90\%$). This necessarily implies an excellent DHR (at least 90% probablity to recognize merged hits). On the other hand only a moderate π-rejection factor is required (a rejection factor of 100-200 is sufficient). Finally an acceptance slightly larger than that of the central arms is highly desirable (e.g. a coverage of $\mid \delta\eta \mid \leq 0.40$ and $\delta\phi \leq 100\,\mathrm{deg}$).

Table 7: Summary of S/B results

		S/B
Present configuration		**1/7**
B = 0 at r $\leq$ 60cm		**1/5**
B =0 + Inner detector:	**no e-ID (cut with all hits)**	**1**
	no e-ID (cut with single hits)	**2**
	e-ID	**12**
	e-ID + veto area	**20**

References

[1] G.E. Brown and Mannque Rho, Phys. Rept. 269, (1996) 333.

[2] J. Wambach and R. Rapp, Nucl. Phys. A638 , (1998) 171.

[3] G. Agakichiev, et al. (CERES Collaboration), Phys. Lett. B422, (1998) 405.

[4] R. Muto, et al. J. Phys. G: Nucl. Part. Phys.30 (2004) S1023

[5] J. Porter et al., Phys.Rev.Lett. 79, (1997) 1229.

[6] Bratkovskaya et al., Nucl.Phys. A634, (1998) 168.

[7] S. Turbide, R. Rapp and C. Gale, Phys. Rev. C69, (2004) 014903.

[8] R.Rapp, nucl-th/0204003 (2002).

[9] M. Gyulassy and L. McLerran, nucl-th/0405013, accepted in Nucl. Phys. A (2004).

[10] E.V. Shuryak and I. Zahed, Phys. Rev. D70, (2004) 054507 and hep-ph/0406100 (2004).

[11] H. Asakawa and T. Hatsuda, Phys.Rev.Lett. 92, (2004) 012001 and Prog. Theor. Phys. Suppl. 149, (2003) 42.

[12] Technical Note 391: Proposal for a Hadron Blind Detector for PHENIX,2001.

[13] F. Sauli, Nucl. Instr. and Meth. A386 (1997), 531

[14] A. Kozlov, I. Ravinovich, L. Shekhtman, Z. Fraenkel, M. Inuzuka and I. Tserruya, Nucl. Instr. and Meth. A523 (2004), 345

[15] Z. Fraenkel et al., submitted to Nucl. Instr. and Meth., January, 2005.

[16] B.Azmoun, N.Smirnov, S.P.Stoll and C.L.Woody, paper N16-49, to be published in the Conference Record Proceedings of the 2004 IEEE Nuclear Science Symposium and Medical Imaging Conference, Rome, Italy, Oct 16-22, 2004.

[17] D. Mörmann, A. Breskin, R. Chechik, P. Cwetanski and B.K. Singh Nucl. Instr. and Meth. A478 (2002), 230.

[18] B.K. Singh, E. Shefer, A. Breskin, R. Chechik and N. Avraham, Nucl. Instr. and Meth. A454 (2000), 364.

[19] Archana Sharma,
http://consult.cern.ch/writeup/garfield/examples/gas/trans2000.html.

[20] A. Breskin, A. Buzulutskov and R. Chechik, Nucl. Instr. and Meth. A483 (2002), 670.

[21] H. Raether, Z. Phys. 112 (1939, 464

[22] D.Mörmann, A.Breskin, R.Chechik, and B.K.Singh, Nucl. Instr. and Meth. A471, (2000), 333.Breskin, R. Chechik and D. Bloch, Nucl. Instr. and Meth. A516 (2004) 315.

[23] A. Bondar, A. Buzulutskov, L. Shekhtman and A. Vasiljev, Nucl. Instr. and Meth. A496 (2003), 325.

[24] F. Sauli, S. Kappler and L. Ropelewski,IEEE Trans.Nucl. Sci. NS-50 (2003) 803.

[25] D. Mörmann, A. Breskin, R. Chechik, P. Cwetanski and B.K. Singh Nucl. Instr. and Meth. A478 (2002), 230

[26] A. Breskin, Nucl. Instr. and Meth. A371 (1996), 116.

[27] B.K. Singh, E. Shefer, A. Breskin, R. Chechik and N. Avraham, Nucl. Instr. and Meth. A454 (2000), 364.

[28] D. Mörmann, A. Breskin, R. Chechik and B.K. Singh, Nucl. Instr. and Meth. A471 (2001), 333

[29] R. Gernhauser et al., Nucl. Instr. and Meth. A371 (1996), 300

[30] A. Pansky et al., Nucl. Instr. and Meth. A354 (1995), 262

[31] M.Hohlmann et al., Proceedings of the Aging Workshop Nucl. Instr. and Meth. A471, (2000), 333.

[32] A reference/report where the change of the GEM gain with time is discussed. It was attributed to the charge built up on the GEM holes surface.

[33] J.Adams et al.(STAR Collab).nucl-ex/0406003.